

Image segmentation of treated and untreated tumor spheroids by Fully Convolutional Networks

Matthias Streller,^{1,2} Soňa Michlíková,^{3,4} Willy Ciecior,^{1,2} Katharina Lönnecke,^{1,2}
Leoni A. Kunz-Schughart,^{3,5} Steffen Lange,^{3,1} and Anja Voss-Böhme^{1,2}

¹DataMedAssist Group, HTW Dresden-University of Applied Sciences, 01069 Dresden, Germany

²Faculty of Informatics/Mathematics, HTW Dresden-University of Applied Sciences, 01069 Dresden, Germany

³OncoRay - National Center for Radiation Research in Oncology,
Faculty of Medicine and University Hospital Carl Gustav Carus,

TUD Dresden University of Technology, Helmholtz-Zentrum Dresden-Rossendorf, Dresden, Germany

⁴Helmholtz-Zentrum Dresden-Rossendorf, Institute of Radiooncology - OncoRay, Dresden, Germany

⁵National Center for Tumor Diseases Dresden (NCT/UCC),

Germany: German Cancer Research Center (DKFZ), Heidelberg,

Germany; Faculty of Medicine and University Hospital Carl Gustav Carus, TUD Dresden University of Technology,
Dresden, Germany; Helmholtz-Zentrum Dresden-Rossendorf (HZDR), Dresden, Germany

Background and objectives Multicellular tumor spheroids (MCTS) are advanced cell culture systems for assessing the impact of combinatorial radio(chemo)therapy. They exhibit therapeutically relevant *in-vivo*-like characteristics from three-dimensional (3D) cell-cell and cell-matrix interactions to radial pathophysiological gradients related to proliferative activity and nutrient/oxygen supply, altering cellular radioresponse. The therapeutic outcome of MCTS is most frequently monitored over time via brightfield microscopy imaging. Classical yet non-curative analytical readouts relate to spheroid size and volume growth kinetics. State-of-the-art assays also quantify long-term curative endpoints based on collected image time series from large treated spheroid populations per irradiation dose and treatment arm. Here, spheroid control probabilities are documented analogous to *in-vivo* tumor control probabilities based on Kaplan-Meier curves. These analyses require spheroid segmentation to extract relevant structural information from the images, e.g., diameter, area, volume and circularity. This laborious process entails manual inspection and analysis of up to 100.000 images per treatment arm. While several image analysis algorithms are available for spheroid segmentation, they all focus on compact MCTS with clearly distinguishable outer rim throughout growth. However, treated MCTS may partly be detached and destroyed and are usually obscured by dead cell debris. Thus, this work aims to develop an advanced automatic segmentation that also covers the previously neglected cases of spheroids obstructed by debris.

Methods We successfully train two Fully Convolutional Networks, UNet and HRNet, and optimize their hyperparameters to develop an automatic segmentation for both untreated and treated MCTS. We systematically validate the automatic segmentation on larger, independent data sets of spheroids derived from two human head-and-neck cancer cell lines.

Results We find an excellent overlap between manual and automatic segmentation for most images, quantified by Jaccard indices at around 90%. For images with smaller overlap of the segmentations, we demonstrate that this error is comparable to the variations across segmentations from different biological experts, suggesting that these images represent biologically unclear or ambiguous cases.

Conclusion The developed automatic segmentation cannot only be used directly but also integrated into existing spheroid analysis pipelines and tools. This facilitates the analysis of 3D spheroid assay experiments and contributes to the reproducibility and standardization of this preclinical *in-vitro* model.

I. INTRODUCTION

One of the most challenging problems in oncology is the development of therapeutic approaches for tumor growth suppression and eradication, as well as designing and optimizing treatment protocols. In this context, three-dimensional (3D) multicellular tumor spheroids (MCTS) are an advocated pre-clinical, *in-vitro* model to systematically study possible means of tumor suppression, assess the curative effect of combinatorial radio(chemo)therapy, and predict the response of *in-vivo* tumors [1–8]. In contrast to two-dimensional (2D) clonogenic survival assays, which are known to reflect the therapeutic response of cancer cells in the tissue comparatively poorly [9] multicellular spheroids are reproducible 3D avascular clusters of several thousand

tumor cells without or in advanced settings with stromal cell compartments mimicking the pathophysiological milieu of tumor microareas or micrometastases. Due to their more or less radial 3D histomorphology and structure, they exhibit many characteristic features affecting tumor growth dynamics, including 3D reciprocal cell-cell and cell-extracellular-matrix interactions as well as metabolic gradients of oxygen, nutrients and waste products, which strongly impair the cells' proliferative activity and therapy response [4–8], in particular oxygen deficiency (hypoxia), which is associated with substantial radioresistance [10–13]. After a long phase in which spheroids were used only in specialized laboratories, methodological advances in serial culturing and live imaging have led to an exponential spread of this *in-vitro* model system over the past two decades [7, 8, 14].

While 3D tumor spheroids provide a physiologically more realistic *in-vitro* framework to study tumor growth dynamics and therapeutic outcomes, the analysis of the experiments is much more complex than for traditional 2D cultures. 3D tumor spheroids’ dynamics with and without treatment are most frequently monitored via microscopy imaging. State-of-the-art long-term spheroid-based assays assess therapy response from these image time series by classifying each spheroid within a population as either controlled or relapsed based on their growth kinetics. By averaging the therapeutic response over ensembles of spheroids for each treatment dose, the spheroid control probabilities and spheroid control doses are computed as analytical endpoints [15–18], analogous to the tumor control dose employed in *in-vivo* radiotherapy experiments with tumor-bearing mice [19, 20]. Moreover, time points of relapse are identified to quantify growth recovery in terms of Kaplan-Meier curves. These metrics depend on the spheroid type (cell line), the size of the spheroids at the onset of treatment, and the applied treatment and often require the extraction of growth curves, i.e., spheroid volume over time, from the image time series of all individual spheroids.

The associated data analysis poses a significant, interdisciplinary challenge: A single, typical experimental series of a long-term spheroid-based assay, i.e., 2-3 cell models at ten different doses with 3-5 agents and 30 spheroids per treatment arm monitored up to 60 days after treatment, generates up to 10^5 images. In the past, several tools were developed for spheroid image analysis [21–26], including SpheroidSizer [27], AnaSP [28, 29], TASI [30], SpheroidJ [31], and INSIDIA [25, 32]. The most crucial part of spheroid image analysis is the identification of the set of pixels in an image that corresponds to the spheroid, as this forms the basis for the extraction of spheroid characteristics like diameter, volume, and circularity as well as other morphologic features. This identification or classification of pixels in a given image is denoted semantic image segmentation [33] and represents the greatest challenge in spheroid image analysis. Previous spheroid segmentations were based on classical segmentation techniques, including thresholding methods (Yen [34], Otsu [28, 35]), watershed algorithm [36], shape-based detections (Hough transform algorithms [37], active contour models/snake [38]), or edge detection (Canny, Sobel [31]), and are also available as ImageJ plugins [22, 25], Matlab packages [27, 28, 30] or dedicated segmentation programs [39–41]. Since characteristics of spheroid images, including the size, shape, and texture of the actual spheroid, vary with cell line, treatment, and microscopy method (brightfield [25, 29, 31, 32, 42], fluorescence [25, 26, 31, 32, 43, 44], differential, interference contrast [45]), most of these approaches and tools are specialized for certain experimental conditions or even concrete microscopes [43, 44] and often fail to generalize to arbitrary conditions. In the recent years, data-based methods especially deep-learning models have been increasingly employed for spheroid segmentation to tackle this issue of generalization [29, 31, 42, 45–48]. Deep-learning segmentation also allows more complex analysis, e.g., identification of time-lapse migratory patterns [45] or distinction of spheroids’ core and invasive edge [32].

However, these segmentation and analysis tools have primarily been developed for experimental conditions where the resulting images are relatively clean with well-visible, unobstructed MCTS. In contrast, radiotherapy, one of the most common cancer treatments, regularly causes spheroids to shed dead cells or even to detach completely. Consequently, dead cell debris often obscures the remaining shrunk MCTS and the 3D cultures putatively regrowing from surviving viable cells after detachment, see Fig. 1 for two examples. This debris can cover a much larger domain than the actual spheroid and can be locally even thicker and thus darker, which makes segmentation difficult even for human experts. Both classical segmentation techniques and previous deep-learning models trained on compact spheroids typically fail in these cases or require manual adjustments for individual images.

We train deep-learning models to segment spheroid images after radiotherapy based on annotated images from a previous experiment assessing the radioresponse of human head-and-neck squamous cell carcinoma (HNSCC). After systematic optimization of hyperparameters and pre-processing for two selected network architectures, U-Net and HRNet, the automatic segmentation exhibits high accuracy for images of both treated and untreated spheroids. We further validate the automatic segmentation with the optimized U-Net on larger, independent data sets of two cell types of head-and-neck cancer exposed to both radiotherapy and hyperthermia. For the majority of images, we find excellent overlap between manual and automatic segmentation, even in the case of small, heavily obstructed spheroids, see Fig. 1. In particular, we compare segmentations of different biological experts and find that imprecisions of the automatic segmentation are comparable to variations across different humans. The optimized automatic segmentation is provided in a minimal tool with a graphical user interface.

II. MATERIALS

The original data set consists of several image time series of spheroids of the head-and-neck cancer cell line FaDu [16], which is one of the two cell lines from this previously published study on radioresponse of human head-and-neck cancer: Each spheroid was irradiated with a photon beam at single dose of either 2.5 Gy, 5.0 Gy, 7.5 Gy or 10.0 Gy, with each dose being represented approximately equally in the data set, and imaged for up to 60 days after treatment with brightfield microscopy. 1095 spheroids were manually segmented by a biological expert (human H1) to train and test the fully convolutional networks (FCNs). These annotated data are split into 3 separate data sets: 883 images for training, 108 images for validation, and 104 images for testing. Images from a single spheroid are assigned to one of the groups exclusively, to rule out unwanted correlations between training, validation, and testing data set. For further testing another set of 6574 images of head-and-neck cancer (FaDu and SAS) spheroids from the same study [16], treated with different combinations and doses of x-ray irradiation and hyperthermia, is manually segmented by several biolog-

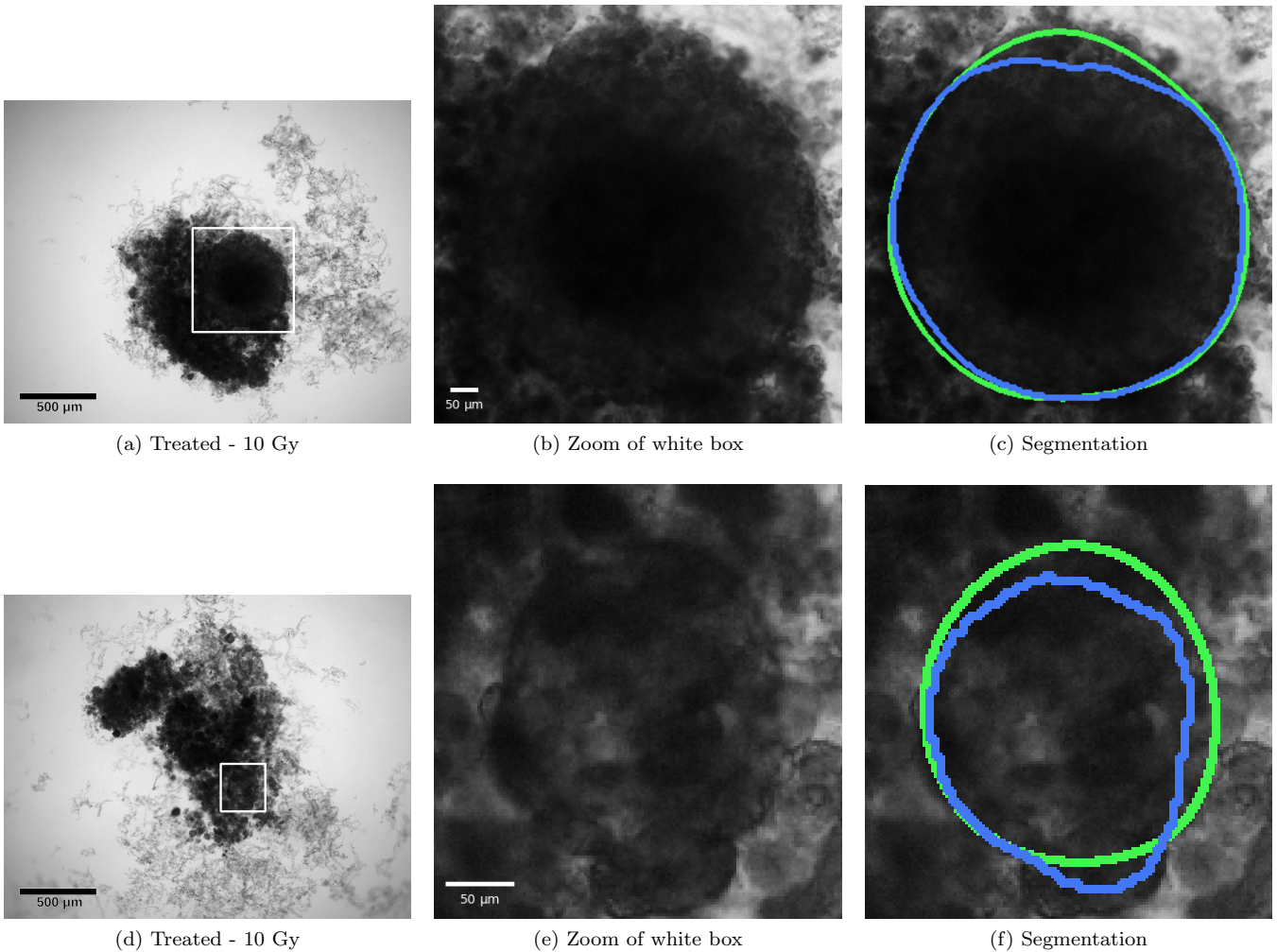


FIG. 1. Representative examples of images for automatic segmentation with the optimized U-Net (blue) compared to the manual segmentation (green) for 3D tumor spheroids after treatment. The overlap with the manual segmentation is excellent for standard size and larger spheroids obscured by cell debris (top row) and sufficient for small, heavily obscured spheroids (bottom row). Displayed are (a,d) the original images, which are also the input for the U-Net, (b,d) magnified image details around the spheroids as indicated by the white box in (a,d) for visibility, and (c,e) corresponding contours from the segmentations. The metrics for evaluation of the automatic segmentation are: the top row - JCD = 7.6%, RDD = 3.7% and RCD = 1.6%; bottom row - JCD = 22.7%, RDD = 7.5% and RCD = 14.7%, see text for details.

ical experts independently (humans H2-H5). Note that while the automatic segmentation is performed on individual images, biological experts always take previous and subsequent images of a spheroid into account for manual segmentation.

The original images were taken with a Zeiss Axiovert 200M at a resolution of 1300×1030 pixels representing $2.04 \mu\text{m}/\text{pixel}$ with 16-bits gray-scale per pixel [16]. Images are converted to 8-bit images to ensure compatibility with the employed libraries FastAi [49] and SemTorch [50]. While this conversion in principle reduces the contrast level, this effect is negligible as only a small fraction of the 16-bit range is utilized during imaging, e.g., the mean gray-scale value in the images is 1300 ± 130 , and values are rescaled such that smallest gray-scale value of the original image becomes 0 and the biggest value becomes 255.

As deep-learning models, we use FCNs a particular group

of convolutional neural networks intended for semantic image segmentation [51], in particular the U-Net [52] and the HRNet [53]. The U-Net is one of the most established FCN frameworks. The HRNet has a special architecture compared to other typical FCN models and has been already successfully employed in the case of clean images with clearly visible spheroids [31]. The pipeline to train the models employs FastAi [49] for the U-Net and its backbones and SemTorch [50] for the HRNet. Before each training a suitable learning rate is picked using LR Range [54]. The training follows the 1-cycle policy: the learning rate is cycled once between two bounds, which allows a fast convergence [54]. A callback stops the training, if the accuracy of the segmentation reaches its peak. The models are trained on a GPU NVIDIA GeForce RTX 3080 with a mini batch size of 2. For training on images with higher resolution or to compare

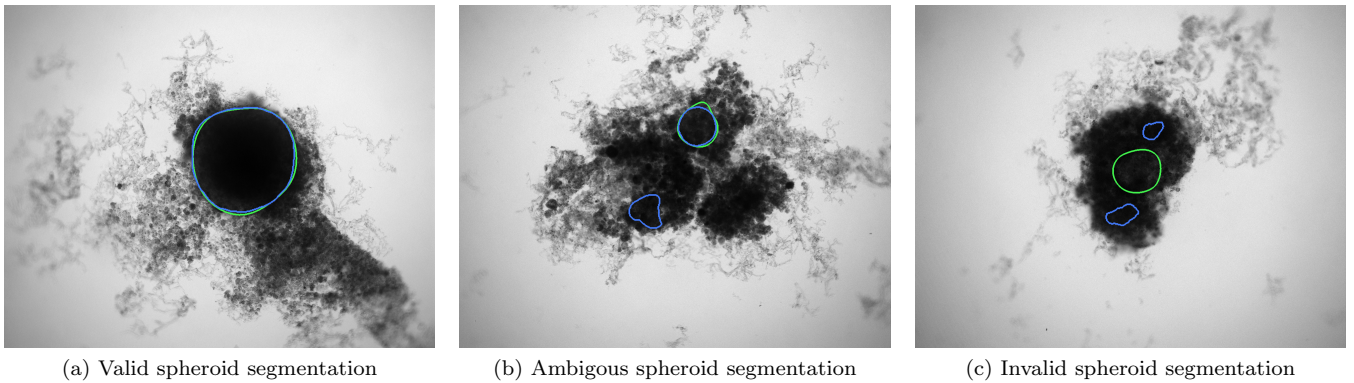


FIG. 2. Exemplary evaluation of the automatic segmentation (blue) with respect to the manual one (green) for (a) standard case and (b),(c) rare artifacts, see text for details: (a) Spheroid is correctly segmented: no contribution to ISF or ASF; JCD, RDD and RCD are well defined. (b) Excessive spheroids are detected beyond the actual spheroid: no contribution to ISF, one count added to ASF; JCD, RDD and RCD are well defined and computed for the larger, upper spheroid. (c) No overlap between automatic and manual segmentation: one count added to ISF, no contribution to ASF; JCD, RDD and RCD are set to one.

some specific backbones, online learning is used instead of mini batches to avoid memory overflow.

III. METHODS

The segmentation is evaluated via several metrics (Section III A: Jaccard Distance (JCD), Relative Diameter Deviation (RDD), Relative Circularity Deviation (RCD), Ambiguous Spheroid Fraction (ASF), Invalid Spheroid Fraction (ISF)) additional to the standard accuracy quantified by the Jaccard coefficient of the whole data set, which is used during training. These metrics are computed for individual images to report not only their mean values but also their deviations, and thus reliability, across the test data set. These metrics are used to optimize the hyperparameters, Section III B, and data augmentation, Section III C, of the selected FCN models U-Net and HRNet for maximal accuracy.

A. Evaluation metrics

Several metrics are employed to assess the accuracy of the segmentation. The most important one is the Jaccard Distance (JCD), which measures the relative difference between two sets of pixel P and T ,

$$\text{JCD} = 1 - \text{IoU} = 1 - \frac{|P \cap T|}{|P \cup T|}. \quad (1)$$

with the automatically segmented (predicted) pixel set P from the FCN and the (target) pixel set T of the manually segmented spheroid. Note that in the literature often the opposite Intersection over Union metric $\text{IoU} = 1 - \text{JCD}$ also called Jaccard index, or Jaccard similarity coefficient, is used. The JCD takes values between 0 (automatic segmentation perfectly overlaps with the manual one) and 1 (no intersection between the two segmentations). The JCD can

be understood as the relative area error of the segmentation, i.e., in the example of Fig. 2a $\text{JCD} = 0.042$ is obtained, which means 4.2% error in the segmented area. A selection of sample images with different JCDs is displayed in SI Figs. 1-3 to give an optical reference for this metric. From these sample images and in accordance with the biological experts, it may be concluded that a JCD below 0.2 is justifiable and such a deviation is observed between segmentations of different humans, see also Section IV C.

It is possible that the spheroid is correctly segmented, but additionally another non-existent spheroid is detected, see Fig. 2b, where additionally to the manually segmented spheroid in the top right another contour in the bottom left is suggested by the automatic segmentation. In this case, the JCD would be below 1 but differ from 0. The fraction of these cases among all images are additionally denoted Ambiguous Spheroid Fraction (ASF). Furthermore, a JCD of 1 can mean that the spheroid is found in the wrong place or the spheroid is not found at all, see Fig. 2c. The fraction of these cases is denoted Invalid Spheroid Fraction (ISF).

In practice, only the average diameter $d_T = 2\sqrt{|T|/\pi}$ of the segmented spheroid is extracted to estimate the three-dimensional volume $\pi d_T^3/6$ of the spheroid under the assumption of a spherical shape. Additionally, the circularity $4\pi|T|/L^2$ of the spheroid is computed from its area $|T|$ and perimeter L to assess the validity of this assumption. Thus, we also assess the automatic segmentation by the resulting error of these two values and measure the Relative Diameter Deviation (RDD) and Relative Circularity Deviation (RCD) between the segmentations

$$\text{RDD} \triangleq \text{RCD} = \frac{|c_P - c_T|}{c_T} \quad (2)$$

where c_P is either mean diameter or circularity based on the automatic segmentation and c_T is the corresponding characteristic calculated based on the manual segmentation. In case of several spheroids the predicted spheroid with the

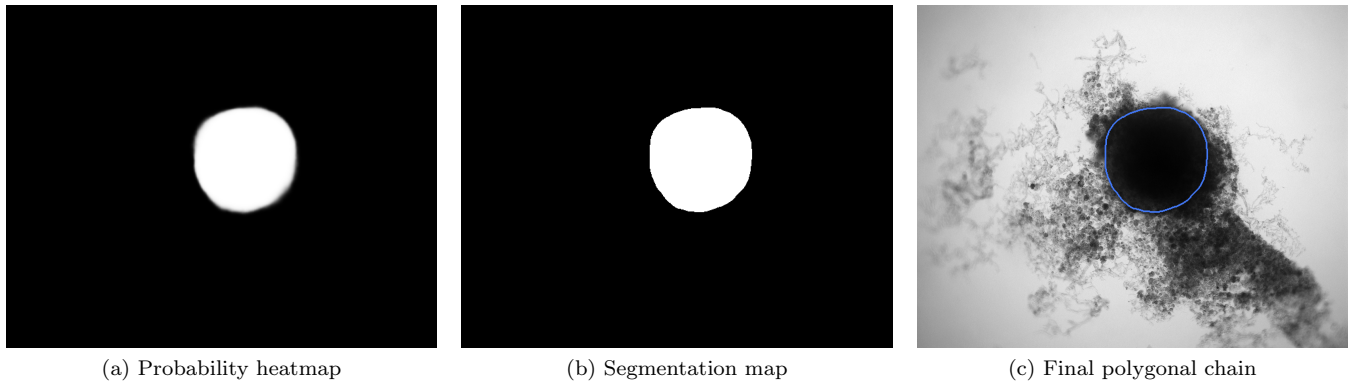


FIG. 3. Post-processing steps for the output of the FCN model to transform probability heatmap to spheroid contour: (a) Probability heatmap as output of the FCN model. Each pixel takes probability values between 0 (black) and 1 (white) for being within the a spheroid. (b) By using a threshold of 0.5, the pixels are classified into outside spheroid (black) and inside spheroid (white). (c) Contour of the spheroid border extracted as a polygonal chain (blue line displayed on original image).

highest degree of overlap with the true spheroid is picked for the calculation. In the case of $JCD = 1$, which corresponds to an invalid spheroid, RDD and RCD are also set to 1. The combination of the JCD, ASF, ISF, RDD, and RCD quantify the accuracy of the segmentation with the FCN, where always a value closer to zero means higher agreement between the segmentations.

The spheroid’s pixel set and perimeter are required to calculate the metrics. Thus, probability heatmaps, created by the Softmax function in the last layer of the FCN, are transformed into binary images and polygonal chains as illustrated in Fig. 3. First, the binary image is created. For this purpose, every pixel with a probability value higher or equal to 50% will be counted as a spheroid pixel and set to 1. Values of the other pixels are set to 0. The coordinates from the outer border of the emerged shape in the binary image can be extracted by the algorithm proposed in [55], thereby creating the final polygonal chain.

B. Hyperparameter optimization

Several hyperparameters and pre-processing methods can be adjusted to improve the accuracy of the selected FCN models. We successively optimize the most relevant parameters, starting from the ones with the most significant expected impact on accuracy to the one with the lowest impact, i.e., *backbone*, *transfer learning*, *data augmentation*, *input resolution*, *loss function*, and *optimizer*: The *backbone* defines the exact architecture of the FCN model and is accordingly the most important hyperparameter. For *transfer learning* the ImageNet [56] data set is utilized. The *data augmentation* techniques are described in Section III C. Furthermore, the impact of changing the *input resolution* is investigated. Afterward, the *loss function* for quantifying the FCN’s error is optimized, particularly by comparing distribution-based loss and a region-based loss. We pick the Dice loss for region-based loss and the Cross-Entropy loss as a distribution-based loss function. We also test the Focal

loss, which is a variation of Cross-Entropy and suitable for imbalanced class scenarios [33]. Finally, two different optimizers for minimizing the loss function are evaluated. One is Adam [57], a very common optimizer, and the other one is a combination of some more modern optimizers, RAdam [58] and Lockhead [59]. For the backbone, the optimization is initiated with a default setting, i.e., transfer learning, no data augmentation, input resolution half of original image, Cross-Entropy loss function, and Adam optimizer. These initial parameters are then individually optimized in consecutive order.

C. Data Augmentation

Data augmentation is a method to generate additional training data via transformations of the original data set. Since this increases the total amount of training data, data augmentation can improve performance and avoid overfitting [60]. In our case, every original training image is transformed once, doubling the size of the original training data set. For each image in the training data set, one of three transformations is picked randomly using Albumentations [60], i.e., vertical flip, horizontal flip, or rotation by 180° . These transformations are valid, since the spheroids do not have a specific orientation within an image. Note that each of these transformation conserves the original rectangular resolution of the image. This avoids extrapolating pixels on the border of the image, which would be necessary for arbitrary rotation angles and which can lead to additional image artifacts the FCN model would have to be trained for.

IV. RESULTS

A. Hyperparameter optimization

For each hyperparameter set and pre-processing method a model is trained and the performance of these trained models

is compared for the validation data set based on the proposed evaluation metrics from Section III A. For JCD, RDD and RCD not only the average value but also the standard deviation over the whole validation data set is reported to estimate reliability of the segmentation. For the ISF and the ASF the standard error of the mean of the corresponding binomial distribution is reported. All results of the optimization are listed in the SI (SI Figs. 4-13) and briefly discussed in the following.

1. Backbones

For the U-Net, the ResNet 34 and the VGG 19-bn architecture perform best, see App. Fig. 4, with a JCD three times smaller than the worst performing backbones, like AlexNet or SqueezeNet1.0. The two ResNet backbones stand out with a very low ASF. Note that the accuracy of the VGG architectures is improving with increasing number of used layers. The ResNet 34 is the optimal backbone as it not only performs best in virtually every metric, but also requires less computational time than the VGG 19-bn. Note that a previous study on deep-learning models for spheroid segmentation observed a higher performance for ResNet 18 compared to VGG 19 and ResNet 50 [29]. For the HRNet the backbones differ in the number of kernels used and the accuracy increases with the number of kernels, see App. Fig. 5. The W48 backbone is preferential, as it not only performs best in the majority of metrics but also displays the lowest standard deviations.

2. Data augmentation and transfer learning

The combination of data augmentation and transfer learning leads to the best performance for both U-Net and HRNet, see App. Fig. 6 and App. Fig. 7. While this is in principle expected, the improvement is substantial as the JCD is more than halved when both transfer learning and data augmentation is introduced. Note that for the U-Net, transfer learning improves accuracy more than data augmentation, while the opposite is true for the HRNet.

3. Resolution

Using input images with half the resolution 650×515 of the original images leads to the best performance, see App. Fig. 8 and App. Fig. 9. This input resolution is already used to optimize the previous parameters. Higher resolution (3/4, 1) reduces accuracy, presumably because the increase in details makes generalization of the appearance of spheroids more difficult, and the receptive fields of the kernels are getting smaller relative to the whole image. Lower resolution (1/4) also reduces accuracy, presumably due to the loss of relevant information. Half resolution displays the best accuracy and lowest standard deviations across the validation data set.

TABLE I. (a) Evaluation of the segmentation with the optimized U-Net and HRNet models on the test data set shows higher accuracy of the U-Net. Note that all metrics can range between zero and one, where lower values mean higher accuracy and zero means perfect agreement with the manual segmentation. (b) Evaluation of the optimized segmentations on images of untreated (not irradiated) spheroids shows high accuracy also for the established case of clean images without cell debris. The optimized U-Net and HRNet achieve almost equal accuracy. The optimal hyperparameter configuration for the U-Net is Backbone: ResNet 34, Optimizer: RAdam & Lockahead, Loss: Dice, Resize factor: 1/2, Transfer learning: Yes, Data augmentation: Yes. The final hyperparameter configuration for the HRNet is Backbone: W48, Optimizer: Adam, Loss: Cross-Entropy, Resize factor: 1/2, Transfer learning: Yes, Data augmentation: Yes.

Model	JCD	RDD	RCD	ISF	ASF
U-Net	0.062	0.020	0.040	0.000	0.010
±	0.060	0.026	0.034	0.000	0.010
HRNet	0.072	0.028	0.036	0.000	0.010
±	0.100	0.080	0.029	0.000	0.010

(a) Segmentation test data set

Model	JCD	RDD	RCD	ISF	ASF
U-Net	0.028	0.008	0.034	0.000	0.000
±	0.010	0.008	0.032		
HRNet	0.029	0.008	0.033	0.000	0.000
±	0.011	0.007	0.026		

(b) Segmentation images without cell debris

4. Loss

We find the Dice loss to be the optimal loss function for the U-Net, see App. Fig. 10. However, the advantage is much smaller than for previous hyperparameters. It does not suggest a general advantage of region-based loss for the segmentation of spheroids by the U-Net. For the HRNet, there is a more significant difference between the region-based loss and the distribution-based loss, see App. Fig. 11. The Focal loss and the Cross-Entropy loss perform better than the Dice loss - especially, the standard deviations differ by a factor of up to three. One reason for this behavior may be that the Dice loss provides less detailed feedback during training than the distribution-based losses. Cross-Entropy loss and Focal loss achieve nearly the same results, and we choose the default Cross-Entropy loss.

5. Optimizer

In case of the U-Net the difference between the tested optimizers is marginal, see App. Fig. 12. We choose the slightly better performing RAdam combined with Lockahead over the default optimizer Adam. In contrast, the accuracy of the HRNet is much worse for the combined optimizer, see App. Fig. 13. The Adam optimizer is optimal with evaluation metrics 1.5 times better than for the RAdam combined with Lockahead.

B. U-Net vs HRNet

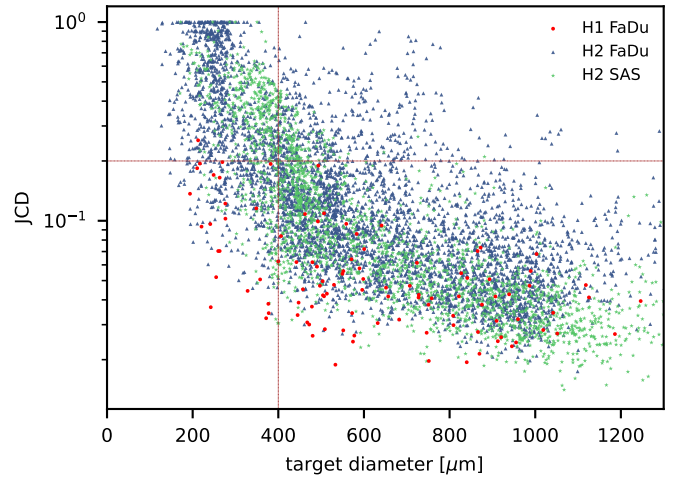
The automatic segmentations with the final optimized U-Net and HRNet model are applied to the test data set. While this test data set is not taken into account during training of the models, the segmentations display virtually the same high accuracy on these new images as for the validation data set, see Tab. IIa and App. Fig. 14 cf. App. Fig. 12 and App. Fig. 13. Mostly, the standard deviations of the metrics are higher in the test data set, though the JCD remains even with this deviation well below 20%. As for the validation data set, the U-Net performs slightly better than the HRNet on the test data. The JCD and RDD for the HRNet are 0.01 higher, and their standard deviation is 0.04 higher. Two representative examples of the automatic segmentation by the U-Net are shown in Fig. 1: The overlap with the manual segmentation is excellent for standard size and larger spheroids obscured by cell debris, see Fig. 1 top row, and sufficient for small, heavily obscured spheroids, see bottom row. In the latter case, the model does not segment the spheroid boundary accurately but detects the spheroid at the correct position $JCD = 23\%$ with a comparable size $RDD = 7.5\%$ within the much larger and often darker cloud of surrounding cell debris. In such difficult cases, similar variations are observed upon manual segmentation by different biological experts.

While the models are mainly trained on images with treated spheroids which are obscured by cell debris, they also accurately segment untreated spheroids with clear boundary and clean background, see Tab. IIb: On a test set of 100 images of untreated spheroids, the accuracy of both models is nearly the same with a JCD below 3%. In comparison, a recent deep-learning approach for spheroids with clear boundary and clean background with focus on generalizability to different experimental conditions and microscopes, achieved a mean JCD of 8% with a standard deviation of 12% for bright-field microscopic images [31]. This suggests that the standard case of clean images without cell debris is included in our training of images with heavily obscured spheroids.

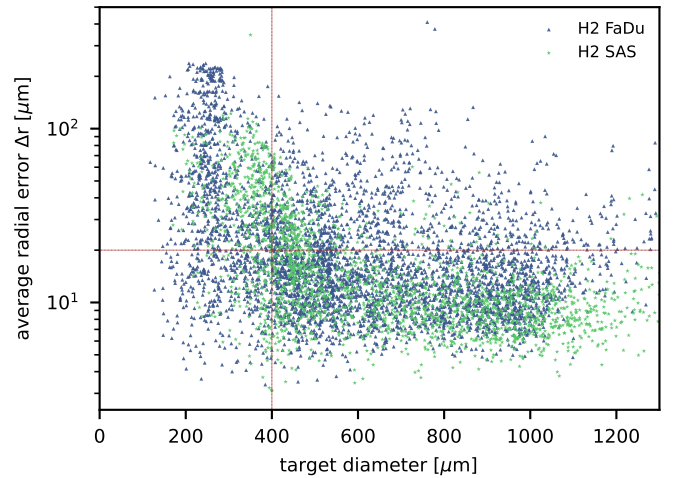
The final U-Net model has a size of 158 MB and the final HRNet model a size of 251 MB. For both models, it takes about 1.8 seconds to segment one image on the CPU (Intel(R) Core(TM) i7-4770). When the segmentation is performed serially on the GPU (NVIDIA GeForce RTX 3080) the U-Net needs only 0.03 seconds per image and the HRNet 0.08 seconds. As computation time for both models is comparable, the U-Net is chosen for the automatic segmentation due to its slightly higher accuracy in our setting. Note that in a recently published deep-learning approach, the comparison of HRNet and U-Net implied that HRNet achieved the highest accuracy [31].

C. Further independent validation

In addition to the standard check with the test data set, we systematically validate the automatic segmentation with the optimized U-Net on larger, independent data sets of two cell types of head-and-neck cancer, see Fig. 4. This data set



(a) JCD over spheroid diameter



(b) Average radial error Δr over spheroid diameter

FIG. 4. Validation of automatic segmentation with the optimized U-Net on larger, independent data sets shows high accuracy for the majority of cases. (a) JCD and (b) average radial error Δr over diameter of the manually segmented (target) spheroid d_T for 6574 images of FaDu (blue triangles) and SAS (green stars) spheroids treated with different combinations and doses of x-ray irradiation and hyperthermia [16]. Manual segmentation is performed by a biological expert (human H2) independently from the manual segmentation (human H1) of the training, validation and test data sets. Results for 104 images of test data set displayed as red dots for comparison. Note that the segmentation is developed only based on images of FaDu spheroids. The majority of deviations are small ($JCD < 0.2$, $\Delta r < 20 \mu\text{m}$, red horizontal lines as guide to the eye), average (median) values are $JCD = 0.17(0.09) \pm 0.2$, $\Delta r = 25(15) \pm 32 \mu\text{m}$ for the whole data set and $JCD = 0.1(0.07) \pm 0.09$, $\Delta r = 18(13) \pm 17 \mu\text{m}$ for spheroids larger $d_T \geq 400 \mu\text{m}$ (red vertical lines as guide to the eye) than the initial, standard size of spheroids. Larger imprecisions for smaller spheroids are due to biologically difficult, unclear or ambiguous cases, see text.

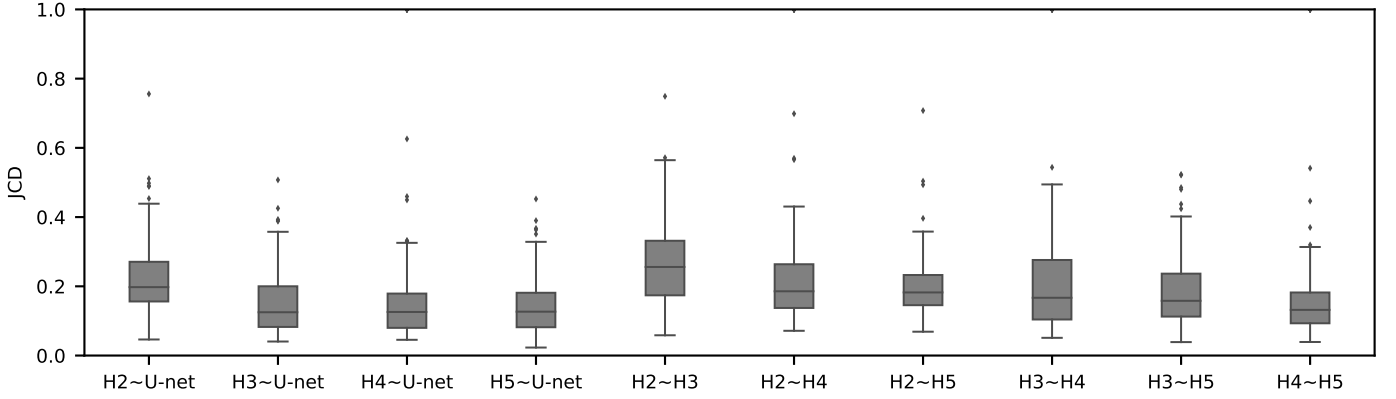


FIG. 5. For spheroids after treatment smaller than the initial, standard size before treatment $d \leq 400 \mu\text{m}$ deviations from the manual segmentation are not bigger than variations across different humans, suggesting that segmentation of images with small spheroids embedded in heavy debris are often difficult to segment or ambiguous. Compared are segmentations from the optimized U-Net and 4 independent human experts (H2-H5) for the same 101 images, which are randomly selected from the pool of small spheroids of the extended validation data set, see Fig. 4. The Friedman test score of all JCDs 217.2 ($p \ll 0.001$) indicates significant differences among the pair-wise segmentation deviations. The order according to the average JCD is (from low to high values) H5~U-Net, H3~U-Net, H3~H5, H2~H5, H4~H5, H4~U-Net, H2~U-Net, H3~H4, H2~H4, H2~H3, where the < indicates a significant ($p < 0.005$) difference between the sets of JCDs according to a Dunn-Bonferroni pairwise post-hoc test.

contains 6574 images of FaDu or SAS spheroids treated with different combinations and doses of x-ray irradiation and hyperthermia [16]. These images were manually segmented by another biological expert (human H2) independent from the original training/validation/test-data set used to develop the automatic segmentation (human H1). For the majority of images, we find excellent overlap between this manual and the automatic segmentation, quantified by a JCD around 0.1, see Fig. 4a. Larger deviations are mostly observed for images with smaller spheroids, i.e., below the size of standard spheroids for treatment (diameter $370 - 400 \mu\text{m}$ according to [15–17]). To make the evaluation intuitive for the biological experts, who are less familiar with the JCD defined in Eq. (1), we additionally introduce a measure of the average radial error Δr based on the automatically segmented (predicted) domain P and the manually segmented (target) domain T

$$\Delta r = \sqrt{\pi^{-1} (|P \cup T| - |P \cap T|) + \frac{d_T^2}{4}} - \frac{d_T}{2} \quad (3)$$

with the average (target) diameter d_T of the manually segmented domain. The error Δr quantifies the thickness a circular layer with the size of the mismatched area $|P \cup T| - |P \cap T| = |P \setminus T| + |T \setminus P|$ around a circle with the target area $|T|$ would have, see App. Fig. 15 for an illustration. Since additional $P \setminus T$ and missing areas $T \setminus P$ do not compensate each other in Eq. (3), the error Δr is considerably larger than the radial error implied by the relative difference between target and predicted diameter RDD, see App. Fig. 16. The average radial error Δr reported in Fig. 4b assesses the segmentation analogous to the JCD with majority of errors $\Delta r < 20 \mu\text{m}$ and larger deviations mostly for spheroids with diameter clearly smaller than before treatment ($d_T \leq 370 - 400 \mu\text{m}$). For reference, note that the resolution of the images is $2.04 \mu\text{m}/\text{px}$, i.e., a deviation of

$20 \mu\text{m}$ corresponds to 10px ($< 1\%$ deviation with respect to the original 1300×1030 image) or 5px in the half-resolution image for application of the U-Net.

Only a few images with larger spheroids exhibit JCD bigger than 0.2. Most of these are ambiguous cases, with two spheroids attached to each other, which are inconsistently recognized as either one or two spheroids even by the human, see examples with $\text{JCD} = 0.28 - 0.34$ and 0.42 in App. Fig. 3. While the training data set did not contain such double-spheroid cases, the optimized U-Net often segments them correctly, see examples with $\text{JCD} = 0.08, 0.12$ in SI Figs. 1 and 2, respectively. Apart from this particular case, most images with larger deviations between the segmentations refers to smaller spheroids with surrounding cell debris. Note that smaller spheroids without cell debris, i.e., untreated or shortly after treatment, do not exhibit such deviations but are accurately segmented. To thoroughly examine these larger deviations in more detail, three biological experts independently segmented 101 randomly selected images with spheroid diameter $d_T \leq 400 \mu\text{m}$. For these 101 images the JCDs between the humans and the U-Net and between different humans are compared in Fig. 5. We find that on average the discrepancies between humans and U-Net are comparable to the variations across segmentations from different humans. This implies that these images represent biologically difficult, unclear, or ambiguous cases. It suggests that the larger JCD observed for some smaller spheroids rather reflects this uncertainty and not a low performance of the U-Net. Accordingly, the evaluation in Fig. 4 refers to a worse-case scenario, as for each spheroid, the biological expert intentionally segmented all images over time, while in practice, segmentation is only required and performed for a fraction of these images, in particular for clearly distinguishable and larger spheroids.

V. DISCUSSION

We develop an automatic segmentation for images of 3D tumor spheroids both with and without (radio)therapy. We systematically validate the automatic segmentation on larger, independent data sets of two cell types of head-and-neck cancer spheroid types, including combinations with hyperthermia treatment. For most images, we find excellent overlap between manual and automatic segmentation. These include clearly discernable spheroids and the previously neglected cases of spheroids critically obstructed by cell debris. For images showing poor overlap of the segmentations, we demonstrate that this error is comparable to the variations between segmentations from different biological experts. This suggests that considerable deviations between automatic and manual segmentations do not necessarily reflect a low performance of the former but rather a general uncertainty or ambiguity in spheroid identification.

It should be pointed out that the imprecisions of the segmentation have a smaller effect on the quantification of therapy response than suggested by the reported JCD: The most informative parameters in long-term spheroid-based assays are the average diameters, volumes, and circularities of the spheroids. Thus, the relevant metric to estimate the error of the automatic analysis is not the JCD but the RDD and RCD, which are considerably smaller as even an imprecise segmentation can result in the correct size or shape of the spheroid. Furthermore, higher deviations are primarily observed for treated 3D cultures with diameters below the initial diameter of standard spheroids $d_T = 370 - 400 \mu\text{m}$ before treatment. These are usually images of spheroids in the final steps of detachment or before cell re-aggregation, growth recovery, and spheroid relapse. In experimental practice, such cases are typically not segmented as they are less relevant for the analytical endpoints. For instance, computation of growth delay requires accuracy of the spheroid segmentation immediately before treatment (for images without obstructing cell debris) and at large spheroid sizes $d_T > 600 \mu\text{m}$, while the images in between have no impact on the growth delay. Moreover, the validation in Fig. 4 is based on images from the time series of relapsed and controlled spheroids. However, in practical routine, segmentations of complete time series are only performed for growth curves and growth delay assessment in spheroid populations at 100 % growth recovery. The average JCD is substantially smaller if the validation is restricted to these cases.

It is important to note that the initial automatic segmentation is driven by images of only one HNSCC spheroid model (FaDu) with and without treatment. However, we show that it works equally well for spheroids from another cell type (SAS), although these SAS spheroids display a different peripheral shape during regrowth after treatment. Beyond the systematic validation highlighted herein, the automatic segmentation has been continuously tested and applied by several biological/biomedical experts and researchers for over a year during their ongoing experiments and to retrospectively reanalyze MCTS from earlier studies. So far, it has been reported that resegmentation is only necessary in a

small fraction of cases, mainly due to optical artifacts, like out-of-focus images. Overall, the segmentation has in the meantime been successfully applied to numerous untreated multicellular spheroid types of different tumor entities and cell lines, respectively (FaDu, SAS - head and neck; Panc-02(mouse), Panc-1, PaTu 8902 - pancreas; HCT-116, HT29 - colon; A549, NCI-H23, NCI-H460 - lung; BT474 - breast; LNCap, DU145 - prostate; U87-MG, U138-MG, U251-MG - brain/GBM; Hek293 - kidney). These spheroids ranged between $200 - 1000 \mu\text{m}$ in diameter and images were taken at different magnifications and resolutions (e.g., 1300×1030 , 1388×1040 , 1920×1440 , 1920×1216 and $1.6 - 2.6 \mu\text{m}/\text{pixel}$) as single or Z-stack images at diverse microscopic devices (Axiovert 200M, AxioObserver Z1 - both from Zeiss; BioTek Cytation 5 Cell Imaging Multimode Reader - Agilent). Many more spheroid types are in the pipeline for implementation. The developed automatic segmentation has also already been applied to contour the images of selected spheroid types, e.g., FaDu, SAS, Panc-02 or DU145, after various treatments such as radiotherapy (X-ray, proton), hyperthermia, chemotherapy and combinatorial treatment.

While the automatic segmentation has been continuously tested for over a year on different cell lines, microscopes, and treatments, it does not necessarily generalize to arbitrary experimental conditions and imaging, which will be the focus of future improvements. However, this problem of domain shift, which can always arise when a model is applied to data sets with a different data distribution than the training data, is also an ongoing challenge for deep-learning models focused on images with clear spheroids and clean background [48]. In contrast, the focus of this study is the inclusion of the case of treated spheroids surrounded by severe cell debris, which is frequent after treatment but often neglected in automatic segmentation.

The automatic segmentation can be incorporated into existing or future tools for spheroid analysis or medical image analysis as basis for further feature extraction including perimeter, complexity, and multiparametric analysis [46]. The segmentation provides a basis for the development of an automatic classification of spheroid image time series into control and relapse and could support machine learning methods to forecast tumor spheroid fate early. To make the deep-learning model available, we provide a minimal tool with graphical user interface. The ONNX Runtime [61] is used to compile the model and to take it into production.

AVAILABILITY AND REQUIREMENTS

Segmentation tool will be published as open-source repository and is already available at <https://wwwpub.zih.tu-dresden.de/~s6079592/>. Requirements and usage are documented in the provided README and some example images for testing are included in the corresponding folder.

ACKNOWLEDGEMENT

We are grateful to M. Wondrak, S. Al-Jamei, N. El-Refai, R. Joseph, and S. L. Prieto for sharing their expertise on tumor spheroid contouring.

FUNDING

The authors acknowledge that this research has been co-financed by the EU, the European Social Fund (ESF), and by tax funds on the basis of the budget passed by the Saxon state parliament (project SAB-Nr. 100382145) and the Bundesministerium für Bildung und Forschung (BMBF 16dkwn001a/b). The funders had no role in study design, data collection and analysis, decision to publish, or preparation of the manuscript.

DECLARATION OF COMPETING INTEREST

The authors declare that they have no competing interests.

-
- [1] F. Franke, S. Michlíková, S. Aland, L. A. Kunz-Schughart, A. Voss-Böhme, S. Lange, Efficient radial-shell model for 3d tumor spheroid dynamics with radiotherapy, *Cancers* 15 (23) (2023) 5645. doi:10.3390/cancers15235645. URL <https://www.mdpi.com/2072-6694/15/23/5645>
- [2] S. C. Brüningk, P. Ziegenhein, I. Rivens, U. Oelfke, G. ter Haar, A cellular automaton model for spheroid response to radiation and hyperthermia treatments, *Sci. Rep.* 9 (1) (2019) 17674. doi:10.1038/s41598-019-54117-x. URL <https://www.nature.com/articles/s41598-019-54117-x>
- [3] S. C. Brüningk, I. Rivens, C. Box, U. Oelfke, G. ter Haar, 3d tumour spheroids for the prediction of the effects of radiation and hyperthermia treatments, *Sci. Rep.* 10 (1) (2020) 1653. doi:10.1038/s41598-020-58569-4. URL <https://www.nature.com/articles/s41598-020-58569-4>
- [4] S. Riffle, R. S. Hegde, Modeling tumor cell adaptations to hypoxia in multicellular tumor spheroids, *Journal of Experimental & Clinical Cancer Research* 36 (1) (2017) 102. doi:10.1186/s13046-017-0570-9. URL <https://doi.org/10.1186/s13046-017-0570-9>
- [5] R. Leek, D. R. Grimes, A. L. Harris, A. McIntyre, Methods: Using three-dimensional culture (spheroids) as an in vitro model of tumour hypoxia, in: C. Koumenis, L. M. Coussens, A. Giaccia, E. Hammond (Eds.), *Tumor Microenvironment, Advances in Experimental Medicine and Biology*, Springer International Publishing, 2016, pp. 167–196. doi:10.1007/978-3-319-26666-4_10.
- [6] F. Hirschhaeuser, H. Menne, C. Dittfeld, J. West, W. Mueller-Klieser, L. A. Kunz-Schughart, Multicellular tumor spheroids: An underestimated tool is catching up again, *Journal of Biotechnology* 148 (1) (2010) 3–15. doi:10.1016/j.jbiotec.2010.01.012. URL <https://www.sciencedirect.com/science/article/pii/S0168165610000398>
- [7] J. Friedrich, R. Ebner, L. A. Kunz-Schughart, Experimental anti-tumor therapy in 3-d: Spheroids - old hat or new challenge?, *International Journal of Radiation Biology* 83 (11) (2007) 849–871. doi:10.1080/09553000701727531. URL <https://doi.org/10.1080/09553000701727531>
- [8] L. A. Kunz-Schughart, J. P. Freyer, F. Hofstaedter, R. Ebner, The use of 3-d cultures for high-throughput screening: The multicellular spheroid model, *J Biomol Screen* 9 (4) (2004) 273–285. doi:10.1177/1087057104265040. URL <https://doi.org/10.1177/1087057104265040>
- [9] V. M. Pérez-García, G. F. Calvo, J. J. Bosque, O. León-Triana, J. Jiménez, J. Pérez-Beteta, J. Belmonte-Beitia, M. Valiente, L. Zhu, P. García-Gómez, P. Sánchez-Gómez, E. Hernández-San Miguel, R. Hortigüela, Y. Azimzade, D. Molina-García, A. Martínez, A. Acosta Rojas, A. Ortiz de Mendivil, F. Vallette, P. Schucht, M. Murek, M. Pérez-Cano, D. Albillo, A. F. Honguero Martínez, G. A. Jiménez Londoño, E. Arana, A. M. García Vicente, Universal scaling laws rule explosive growth in human cancers, *Nature Physics* (2020) 1–6doi:10.1038/s41567-020-0978-6. URL <https://www.nature.com/articles/s41567-020-0978-6>
- [10] P. Howard-Flanders, T. Alper, The sensitivity of microorganisms to irradiation under controlled gas conditions, *Radiat. Res.* 7 (5) (1957) 518–540. doi:10.2307/3570400. URL <https://www.jstor.org/stable/3570400>
- [11] B. Muz, P. d. I. Puente, F. Azab, A. K. Azab, The role of hypoxia in cancer progression, angiogenesis, metastasis, and resistance to therapy, *Hypoxia med. j.* 3 (2015) 83–92. doi:10.2147/HP.S93413.
- [12] A. Rakotomalala, A. Escande, A. Furlan, S. Meignan, E. Lartigau, Hypoxia in Solid Tumors: How Low Oxygenation Impacts the “Six Rs” of Radiotherapy, *Front. Endocrinol.* 12. URL <https://www.frontiersin.org/articles/10.3389/fendo.2021.742215>
- [13] C. Li, L. Wiseman, E. Okoh, M. Lind, R. Roy, A. W. Beavis, I. M. Pires, Exploring hypoxic biology to improve radiotherapy outcomes, *Expert Rev. Mol. Med.* 24 (2022) e21. doi:10.1017/erm.2022.14.
- [14] A. Peirsman, E. Blondeel, T. Ahmed, J. Anckaert, D. Aude-naert, T. Boterberg, K. Buzas, N. Carragher, G. Castellani, F. Castro, V. Dangles-Marie, J. Dawson, P. De Tullio, E. De Vlieghere, S. Dedeyne, H. Depypere, A. Diosdi, R. I. Dmitriev, H. Dolznig, S. Fischer, C. Gespach, V. Goossens, J. Heino, A. Hendrix, P. Horvath, L. A. Kunz-Schughart, S. Maes, C. Mangodt, P. Mestdagh, S. Michlíková, M. J. Oliveira, F. Pampaloni, F. Piccinini, C. Pinheiro, J. Rahn, S. M. Robbins, E. Siljamäki, P. Steigemann, G. Sys, S. Takayama, A. Tesei, J. Tulkens, M. Van Waeyenberge, J. Vandesompele, G. Wagemans, C. Weindorfer, N. Yigit, N. Zablosky, M. Zaroni, P. Blondeel, O. De Wever,

- Mispheroid: a knowledgebase and transparency tool for minimum information in spheroid identity, *Nat Methods* 18 (11) (2021) 1294–1303. doi:10.1038/s41592-021-01291-4.
URL <https://www.nature.com/articles/s41592-021-01291-4>
- [15] O. Chen, F. Manig, L. Lehmann, N. Sorour, S. Löck, Z. Yu, A. Dubrovskaya, M. Baumann, B. M. Kessler, O. Stasyk, L. A. Kunz-Schughart, Dual role of er stress in response to metabolic co-targeting and radiosensitivity in head and neck cancer cells, *Cell. Mol. Life Sci.* 78 (6) (2021) 3021–3044. doi:10.1007/s00018-020-03704-7.
URL <https://doi.org/10.1007/s00018-020-03704-7>
- [16] O. Chen, S. Michlíková, L. Eckhardt, M. Wondrak, A. M. De Mendoza, M. Krause, D. D. McLeod, L. A. Kunz-Schughart, Efficient heat shock response affects hyperthermia-induced radiosensitization in a tumor spheroid control probability assay, *Cancers* 13 (13) (2021) 3168. doi:10.3390/cancers13133168.
URL <https://www.mdpi.com/2072-6694/13/13/3168>
- [17] C. N. Hinrichs, M. Ingarciola, T. Käubler, S. Löck, A. Temme, A. Köhn-Luque, A. Deutsch, O. Vovk, O. Stasyk, L. A. Kunz-Schughart, Arginine deprivation therapy: Putative strategy to eradicate glioblastoma cells by radiosensitization, *Mol Cancer Ther* 17 (2) (2018) 393–406. doi:10.1158/1535-7163.MCT-16-0807.
URL <https://mct.aacrjournals.org/content/17/2/393>
- [18] B. Vynnytska-Myronovska, Y. Bobak, Y. Garbe, C. Dittfeld, O. Stasyk, L. A. Kunz-Schughart, Single amino acid arginine starvation efficiently sensitizes cancer cells to canavanine treatment and irradiation, *International Journal of Cancer* 130 (9) (2012) 2164–2175. doi:10.1002/ijc.26221.
URL <https://onlinelibrary.wiley.com/doi/abs/10.1002/ijc.26221>
- [19] B. Kummer, S. Löck, K. Gurtner, N. Hermann, A. Yaromina, W. Eicheler, M. Baumann, M. Krause, C. Jentsch, Value of functional in-vivo endpoints in preclinical radiation research, *Radiotherapy and Oncology* 158 (2021) 155–161. doi:10.1016/j.radonc.2021.02.024.
URL <https://www.sciencedirect.com/science/article/pii/S0167814021060874>
- [20] M. Baumann, C. Petersen, M. Krause, Tcp and ntcp in pre-clinical and clinical research in europe, *Rays* 30 (2) (2005) 121–126.
- [21] M. T. Hoque, L. C. E. Windus, C. J. Lovitt, V. M. Avery, Pcaanalyser: A 2d-image analysis based module for effective determination of prostate cancer progression in 3d culture, *PLoS ONE* 8 (11) (2013) e79865. doi:10.1371/journal.pone.0079865.
URL <https://journals.plos.org/plosone/article?id=10.1371/journal.pone.0079865>
- [22] D. P. Ivanov, T. L. Parker, D. A. Walker, C. Alexander, M. B. Ashford, P. R. Gellert, M. C. Garnett, Multiplexing spheroid volume, resazurin and acid phosphatase viability assays for high-throughput screening of tumour spheroids and stem cell neurospheres, *PLoS ONE* 9 (8) (2014) e103817. doi:10.1371/journal.pone.0103817.
URL <https://journals.plos.org/plosone/article?id=10.1371/journal.pone.0103817>
- [23] F. Monjaret, M. Fernandes, E. Duchemin-Pelletier, A. Argento, S. Degot, J. Young, Fully automated one-step production of functional 3d tumor spheroids for high-content screening, *SLAS Technology* 21 (2) (2016) 268–280. doi:10.1177/2211068215607058.
URL <https://www.sciencedirect.com/science/article/pii/S247263032201384X>
- [24] C. T. Rueden, J. Schindelin, M. C. Hiner, B. E. DeZonia, A. E. Walter, E. T. Arena, K. W. Eliceiri, ImageJ2: Imagej for the next generation of scientific image data, *BMC Bioinformatics* 18 (1) (2017) 529. doi:10.1186/s12859-017-1934-z.
URL <https://doi.org/10.1186/s12859-017-1934-z>
- [25] C. Moriconi, V. Palmieri, R. Di Santo, G. Tornillo, M. Papi, G. Pilkington, M. De Spirito, M. Gumbleton, Insidia: A Fiji macro delivering high-throughput and high-content spheroid invasion analysis, *Biotechnology Journal* 12 (10) (2017) 1700140. doi:10.1002/biot.201700140.
URL <https://onlinelibrary.wiley.com/doi/abs/10.1002/biot.201700140>
- [26] M. E. Boutin, T. C. Voss, S. A. Titus, K. Cruz-Gutierrez, S. Michael, M. Ferrer, A high-throughput imaging and nuclear segmentation analysis protocol for cleared 3d culture models, *Sci Rep* 8 (1) (2018) 11135. doi:10.1038/s41598-018-29169-0.
URL <https://www.nature.com/articles/s41598-018-29169-0>
- [27] W. Chen, C. Wong, E. Vosburgh, A. J. Levine, D. J. Foran, E. Y. Xu, High-throughput image analysis of tumor spheroids: A user-friendly software application to measure the size of spheroids automatically and accurately, *J. Vis. Exp.* (89) (2014) 51639. doi:10.3791/51639.
URL <https://www.ncbi.nlm.nih.gov/pmc/articles/PMC4212916/>
- [28] F. Piccinini, Anasp: A software suite for automatic image analysis of multicellular spheroids, *Computer Methods and Programs in Biomedicine* 119 (1) (2015) 43–52. doi:https://doi.org/10.1016/j.cmpb.2015.02.006.
URL <https://www.sciencedirect.com/science/article/pii/S0169260715000309>
- [29] F. Piccinini, A. Peirsman, M. Stellato, J.-C. Pyun, M. M. Tumedei, M. Tazzari, O. De Wever, A. Tesei, G. Martinelli, G. Castellani, Deep learning-based tool for morphotypic analysis of 3d multicellular spheroids, *J. Mech. Med. Biol.* 23 (6) (2023) 2340034. doi:10.1142/S0219519423400341.
URL <https://www.worldscientific.com/doi/abs/10.1142/S0219519423400341>
- [30] Y. Hou, J. Konen, D. J. Brat, A. I. Marcus, L. A. D. Cooper, Tasi: A software tool for spatial-temporal quantification of tumor spheroid dynamics, *Sci Rep* 8 (1) (2018) 7248. doi:10.1038/s41598-018-25337-4.
URL <https://www.nature.com/articles/s41598-018-25337-4>
- [31] D. Lacalle, H. A. Castro-Abril, T. Randelovic, C. Domínguez, J. Heras, E. Mata, G. Mata, Y. Méndez, V. Pascual, I. Ochoa, SpheroidJ: An open-source set of tools for spheroid segmentation, *Comput. Methods Programs Biomed.* 200 (2021) 105837. doi:10.1016/j.cmpb.2020.105837.
URL <https://www.sciencedirect.com/science/article/pii/S0169260720316709>
- [32] G. Perini, E. Rosa, G. Friggeri, L. Di Pietro, M. Barba, O. Parolini, G. Ciasca, C. Moriconi, M. Papi, M. De Spirito, V. Palmieri, Insidia 2.0 high-throughput analysis of 3d cancer models: Multiparametric quantification of graphene quantum dots photothermal therapy for glioblastoma and pancreatic cancer, *International Journal of Molecular Sciences* 23 (6) (2022) 3217. doi:10.3390/ijms23063217.
URL <https://www.mdpi.com/1422-0067/23/6/3217>
- [33] S. Jadon, A survey of loss functions for semantic segmentation, in: 2020 IEEE Conference on Computational Intelligence in Bioinformatics and Computational Biology

- (CIBCB), 2020, pp. 1–7. doi:10.1109/CIBCB48159.2020.9277638.
- [34] J.-C. Yen, F.-J. Chang, S. Chang, A new criterion for automatic multilevel thresholding, *IEEE Transactions on Image Processing* 4 (3) (1995) 370–378. doi:10.1109/83.366472. URL <https://ieeexplore.ieee.org/document/366472>
- [35] N. Otsu, A threshold selection method from gray-level histograms, *IEEE Transactions on Systems Man and Cybernetics* 9 (1) (1979) 62–66. doi:10.1109/TSMC.1979.4310076. URL <https://ieeexplore.ieee.org/document/4310076>
- [36] J. B. T. M. Roerdink, A. Meijster, The watershed transform: Definitions, algorithms and parallelization strategies, *Fundamenta Informaticae* 41 (1) (2000) 187–228. doi:10.3233/FI-2000-411207. URL <https://content.iospress.com/articles/fundamenta-informaticae/fi41-1-2-07>
- [37] R. O. Duda, P. E. Hart, Use of the hough transformation to detect lines and curves in pictures, *Commun. ACM* 15 (1) (1972) 11–15. doi:10.1145/361237.361242. URL <https://dl.acm.org/doi/10.1145/361237.361242>
- [38] V. Caselles, R. Kimmel, G. Sapiro, Geodesic active contours, *International Journal of Computer Vision* 22 (1) (1997) 61–79. doi:10.1023/A:1007979827043. URL <https://doi.org/10.1023/A:1007979827043>
- [39] L. R. Cisneros Castillo, A.-D. Oancea, C. Stüllein, A. Régnier-Vigouroux, A novel computer-assisted approach to evaluate multicellular tumor spheroid invasion assay, *Sci Rep* 6 (1) (2016) 35099. doi:10.1038/srep35099. URL <https://www.nature.com/articles/srep35099>
- [40] M. Vinci, S. Gowan, F. Boxall, L. Patterson, M. Zimmermann, W. Court, C. Lomas, M. Mendiola, D. Hardisson, S. A. Eccles, Advances in establishment and analysis of three-dimensional tumor spheroid-based functional assays for target validation and drug evaluation, *BMC Biology* 10 (1) (2012) 29. doi:10.1186/1741-7007-10-29. URL <https://doi.org/10.1186/1741-7007-10-29>
- [41] F. Cornelissen, M. Cik, E. Gustin, Phaedra, a protocol-driven system for analysis and validation of high-content imaging and flow cytometry, *SLAS Discovery* 17 (4) (2012) 496–508. doi:10.1177/1087057111432885. URL <https://www.sciencedirect.com/science/article/pii/S247255522076341>
- [42] S. K. Sadanandan, J. Karlsson, C. Wählby, Spheroid segmentation using multiscale deep adversarial networks, in: 2017 IEEE International Conference on Computer Vision Workshops (ICCVW), 2017, pp. 36–41. doi:10.1109/ICCVW.2017.11. URL <https://ieeexplore.ieee.org/document/8265222>
- [43] J. P. Celli, I. Rizvi, A. R. Blanden, I. Massodi, M. D. Glidden, B. W. Pogue, T. Hasan, An imaging-based platform for high-content, quantitative evaluation of therapeutic response in 3d tumour models, *Sci Rep* 4 (1) (2014) 3751. doi:10.1038/srep03751. URL <https://www.nature.com/articles/srep03751>
- [44] F. Piccinini, A. Tesei, M. Zanoni, A. Bevilacqua, Revims: Software tool for estimating the volumes of 3-d multicellular spheroids imaged using a light sheet fluorescence microscope, *BioTechniques* 63 (5) (2017) 227–229. doi:10.2144/000114609. URL <https://www.future-science.com/doi/10.2144/000114609>
- [45] T. K. N. Ngo, S. J. Yang, B.-H. Mao, T. K. M. Nguyen, Q. D. Ng, Y.-L. Kuo, J.-H. Tsai, S. N. Saw, T.-Y. Tu, A deep learning-based pipeline for analyzing the influences of interfacial mechanochemical microenvironments on spheroid invasion using differential interference contrast microscopic images, *Materials Today Bio* 23 (2023) 100820. doi:10.1016/j.mtbio.2023.100820. URL <https://www.sciencedirect.com/science/article/pii/S2590006423002806>
- [46] M. Zhuang, Z. Chen, H. Wang, H. Tang, J. He, B. Qin, Y. Yang, X. Jin, M. Yu, B. Jin, T. Li, L. Kettunen, Anatomysketch: An extensible open-source software platform for medical image analysis algorithm development, *J Digit Imaging* 35 (6) (2022) 1623–1633. doi:10.1007/s10278-022-00660-5. URL <https://doi.org/10.1007/s10278-022-00660-5>
- [47] A. Akshay, M. Katoch, M. Abedi, N. Shekarchizadeh, M. Besic, F. C. Burkhard, A. Bigger-Allen, R. M. Adam, K. Monastyrskaya, A. H. Gheinani, Spheroscan: a user-friendly deep learning tool for spheroid image analysis, *GigaScience* 12 (2023) giad082. doi:10.1093/gigascience/giad082. URL <https://doi.org/10.1093/gigascience/giad082>
- [48] M. García-Domínguez, C. Domínguez, J. Heras, E. Mata, V. Pascual, Deep style transfer to deal with the domain shift problem on spheroid segmentation, *Neurocomputing* 569 (2024) 127105. doi:10.1016/j.neucom.2023.127105. URL <https://www.sciencedirect.com/science/article/pii/S0925231223012286>
- [49] J. Howard, S. Gugger, Fastai: A Layered API for Deep Learning, *Information* 11 (2) (2020) 108. doi:10.3390/info11020108. URL <https://www.mdpi.com/2078-2489/11/2/108>
- [50] D. L. Castillo, Semtorch (2020) [cited 2022-10-25]. URL <https://pypi.org/project/SemTorch/#description>
- [51] J. Long, E. Shelhamer, T. Darrell, Fully convolutional networks for semantic segmentation, *IEEE Computer Society*, 2015, pp. 3431–3440. doi:10.1109/CVPR.2015.7298965. URL <https://www.computer.org/csdl/proceedings-article/cvpr/2015/07298965/120mNy49sME>
- [52] O. Ronneberger, P. Fischer, T. Brox, U-net: Convolutional networks for biomedical image segmentation, in: N. Navab, J. Hornegger, W. M. Wells, A. F. Frangi (Eds.), *Medical Image Computing and Computer-Assisted Intervention - MICCAI 2015, Lecture Notes in Computer Science*, Springer International Publishing, 2015, pp. 234–241. doi:10.1007/978-3-319-24574-4_28.
- [53] J. Wang, K. Sun, T. Cheng, B. Jiang, C. Deng, Y. Zhao, D. Liu, Y. Mu, M. Tan, X. Wang, W. Liu, B. Xiao, Deep high-resolution representation learning for visual recognition, *IEEE Trans. Pattern Anal. Mach. Intell.* 43 (10) (2021) 3349–3364. doi:10.1109/TPAMI.2020.2983686.
- [54] L. N. Smith, A disciplined approach to neural network hyperparameters: Part 1 – learning rate, batch size, momentum, and weight decay (2018). arXiv:1803.09820 [cs, stat], doi:10.48550/arXiv.1803.09820. URL <http://arxiv.org/abs/1803.09820>
- [55] S. Suzuki, K. be, Topological structural analysis of digitized binary images by border following, *Computer Vision, Graphics, and Image Processing* 30 (1) (1985) 32–46. doi:10.1016/0734-189X(85)90016-7. URL <https://www.sciencedirect.com/science/article/pii/0734189X85900167>
- [56] J. Deng, W. Dong, R. Socher, L.-J. Li, K. Li, L. Fei-Fei, Imagenet: A large-scale hierarchical image database, in: 2009 IEEE conference on computer vision and pattern recognition, Ieee, 2009, pp. 248–255.
- [57] D. P. Kingma, J. Ba, Adam: A Method for Stochastic Optimization, arXiv:1412.6980 [cs] (Jan. 2017). doi:10.48550/

- arXiv.1412.6980.
URL <http://arxiv.org/abs/1412.6980>
- [58] L. Liu, H. Jiang, P. He, W. Chen, X. Liu, J. Gao, J. Han, On the Variance of the Adaptive Learning Rate and Beyond, arXiv:1908.03265 [cs, stat] (Oct. 2021). doi:10.48550/arXiv.1908.03265.
URL <http://arxiv.org/abs/1908.03265>
- [59] M. Zhang, J. Lucas, J. Ba, G. E. Hinton, Lookahead Optimizer: k steps forward, 1 step back, in: Advances in Neural Information Processing Systems, Vol. 32, Curran Associates, Inc., 2019.
URL <https://proceedings.neurips.cc/paper/2019/hash/90fd4f88f588ae64038134f1eeaa023f-Abstract.html>
- [60] A. Buslaev, V. I. Iglovikov, E. Khvedchenya, A. Parinov, M. Druzhinin, A. A. Kalinin, Albumentations: Fast and flexible image augmentations, Information 11 (2) (2020) 125. doi:10.3390/info11020125.
URL <https://www.mdpi.com/2078-2489/11/2/125>
- [61] O. R. developers, Onnx runtime, <https://onnxruntime.ai/>, version: 1.11.1 (2021).

Appendix A: Supplemental figures

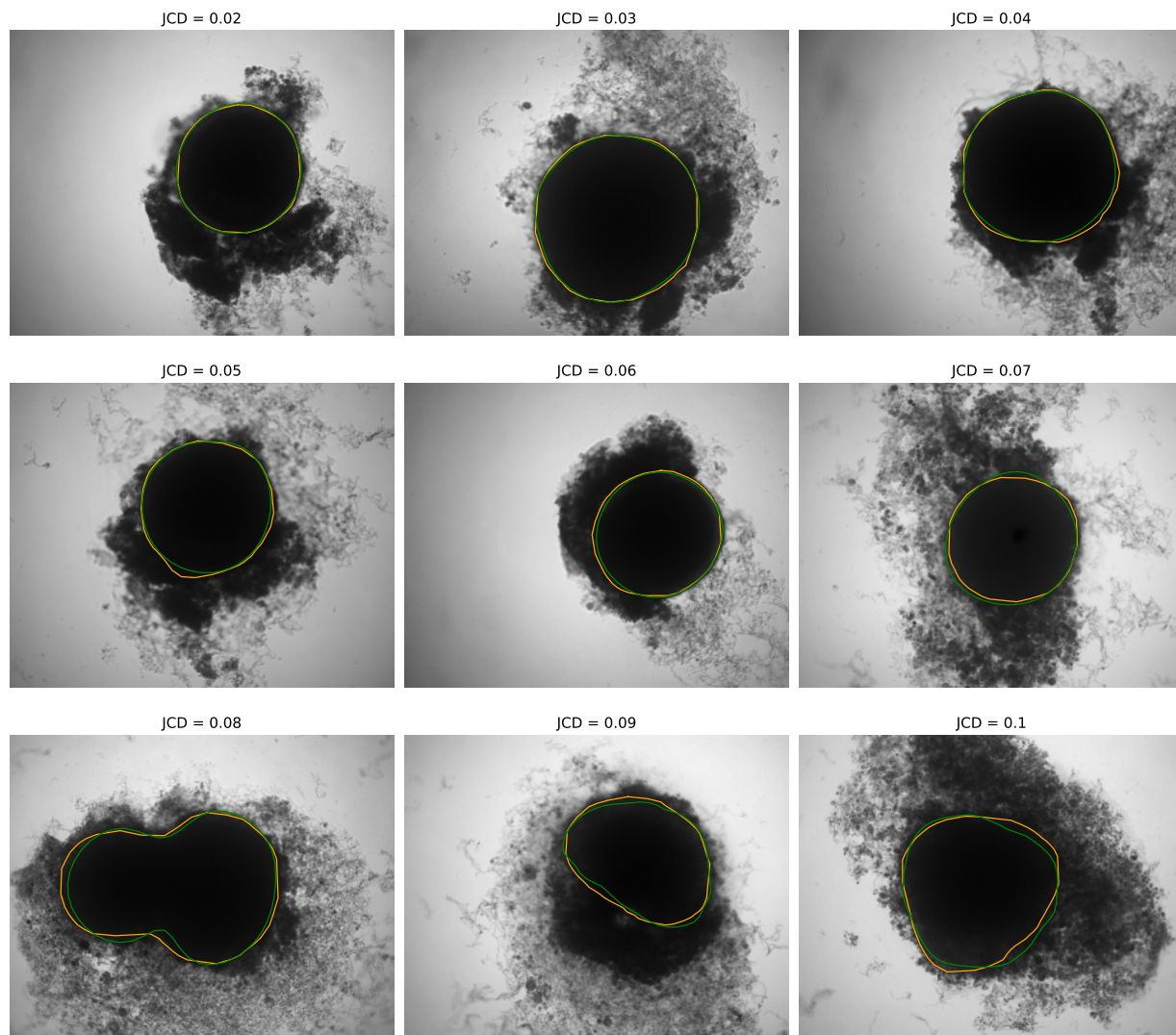


FIG. 1. Selection of sample images as optical reference for $JCD \leq 0.1$ with automatic segmentation from the optical U-Net (orange) and manual segmentation from biological expert H2 (green). From the tested images 52% fall into this range $JCD \leq 0.1$, 67% when only spheroids beyond the standard size $d_T > 400 \mu\text{m}$ are considered. Size of each image corresponds to $2650 \mu\text{m} \times 2100 \mu\text{m}$. Note that the U-Net is trained on an independent manual segmentations from another biological expert H1. Images are selected from the extended validation data set (Fig. 4), in particular, from the subset of larger, better visible spheroids at intermediate levels of debris for visibility. Note that in the example for $JCD = 0.08$ the two attached spheroids are correctly segmented although the training data set does not contain such cases.

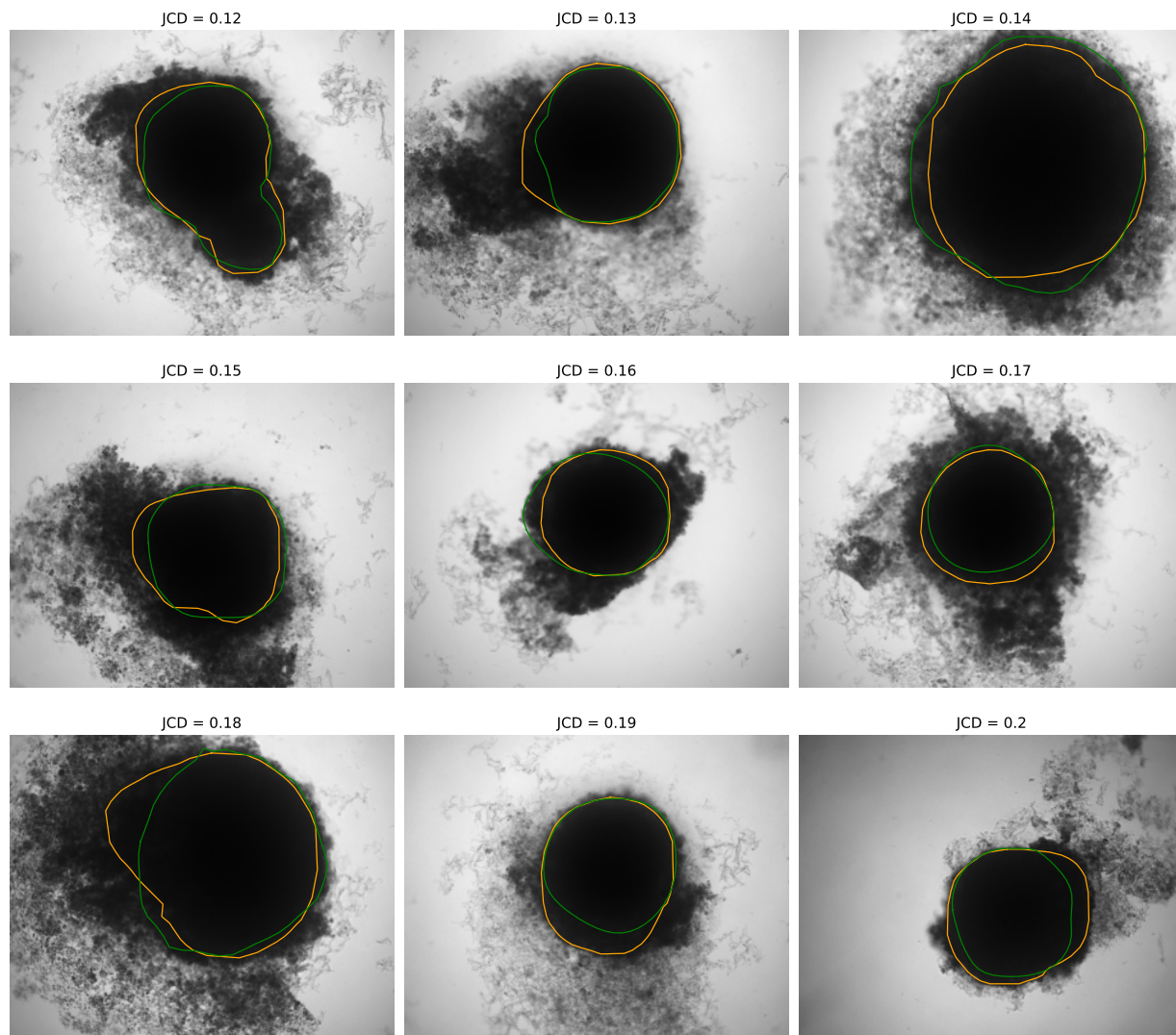


FIG. 2. Selection of sample images as optical reference for $0.1 < \text{JCD} \leq 0.2$ with automatic segmentation from the optical U-Net (orange) and manual segmentation from biological expert H2 (green), analogous to App. Fig. 1. From the tested images 22% fall into this range $0.1 < \text{JCD} \leq 0.2$, 23% when only spheroids beyond the standard size $d_T > 400 \mu\text{m}$ are considered. Note that in the example for $\text{JCD} = 0.12$ the two attached spheroids are correctly segmented although the training data set does not contain such cases.

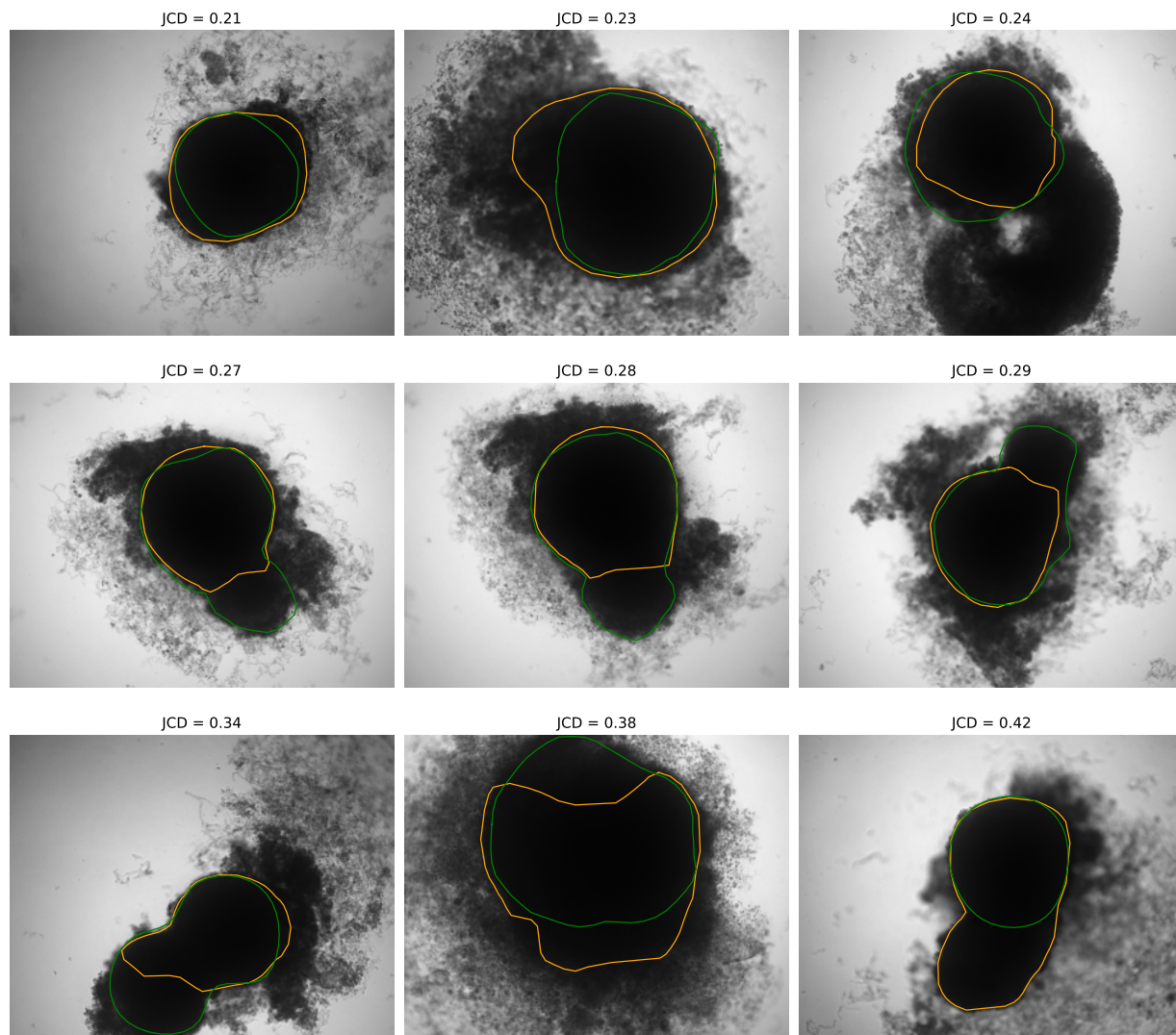
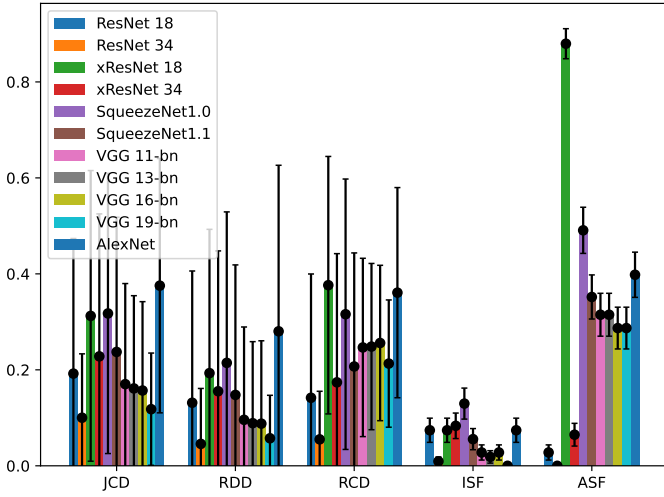
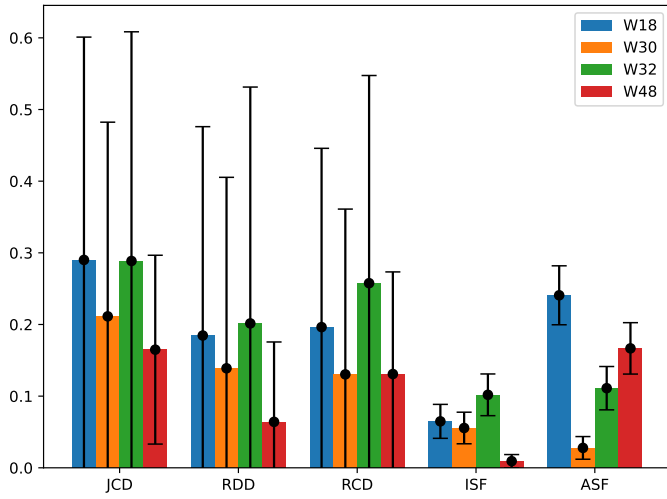


FIG. 3. Selection of sample images as optical reference for larger deviations $JCD > 0.2$ of the automatic segmentation from the optical U-Net (orange) and manual segmentation from biological expert H2 (green), analogous to App. Fig. 1. From the tested images 26% fall into this range $JCD > 0.2$, but merely 10% when only spheroids beyond the standard size $d_T > 400 \mu\text{m}$ are considered. Note that deviations at larger spheroids are often due to cases of double-spheroids, e.g., $JCD = 0.27, 0.28, 0.29, 0.34, 0.42$, which are inconsistently recognized as either one or two spheroids even by the human.



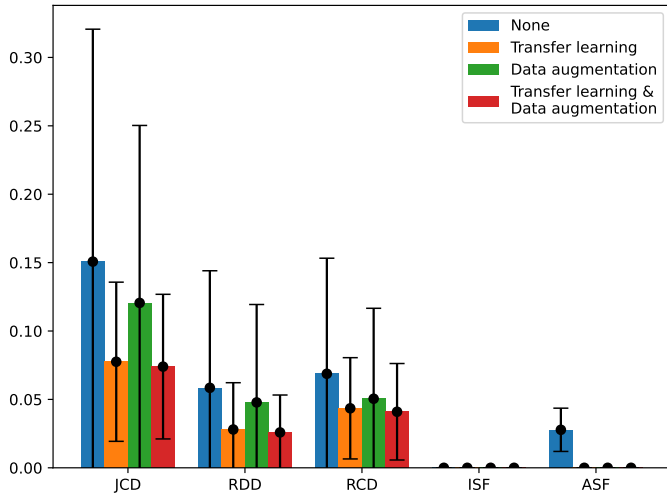
Backbone	JCD	RDD	RCD	ISF	ASF
ResNet 18	0.192	0.131	0.142	0.074	0.028
±	0.282	0.275	0.258	0.025	0.016
ResNet 34	0.100	0.046	0.055	0.009	0.000
±	0.133	0.116	0.100	0.009	0.000
xResNet 18	0.312	0.193	0.376	0.074	0.880
±	0.303	0.300	0.268	0.025	0.031
xResNet 34	0.228	0.155	0.174	0.083	0.065
±	0.297	0.292	0.268	0.027	0.024
SqueezeNet1.0	0.317	0.215	0.316	0.130	0.491
±	0.292	0.315	0.282	0.032	0.048
SqueezeNet1.1	0.237	0.148	0.207	0.056	0.352
±	0.281	0.271	0.237	0.022	0.046
VGG 11-bn	0.170	0.096	0.247	0.028	0.315
±	0.210	0.193	0.186	0.016	0.045
VGG 13-bn	0.161	0.089	0.248	0.019	0.315
±	0.193	0.170	0.173	0.013	0.045
VGG 16-bn	0.157	0.088	0.256	0.028	0.287
±	0.185	0.173	0.162	0.016	0.044
VGG 19-bn	0.118	0.057	0.213	0.000	0.287
±	0.117	0.090	0.133	0.000	0.044
AlexNet	0.375	0.280	0.361	0.074	0.398
±	0.265	0.346	0.219	0.025	0.047

FIG. 4. Values of evaluation metrics for different backbones of the U-Net. Bold values are the best values compared to the other results of one metric. The other hyperparameters are fixed at Optimizer: Adam, Loss: Cross-Entropy, Resize factor: 1/2, Transfer learning: Yes, Data augmentation: No. Overall the ResNet 34 achieved the best results and is picked as the backbone for the U-Net.



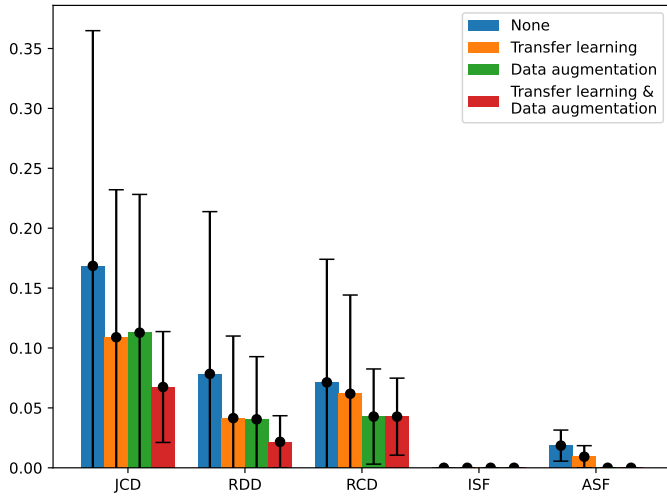
Backbone	JCD	RDD	RCD	ISF	ASF
W18	0.290	0.185	0.196	0.065	0.241
±	0.311	0.291	0.249	0.024	0.041
W30	0.211	0.139	0.130	0.056	0.028
±	0.271	0.266	0.231	0.022	0.016
W32	0.289	0.201	0.258	0.102	0.111
±	0.320	0.330	0.290	0.029	0.030
W48	0.165	0.064	0.131	0.009	0.167
±	0.132	0.111	0.143	0.009	0.036

FIG. 5. Values of evaluation metrics for different backbones of the HRNet. Bold values are the best values compared to the other results of one metric. The other hyperparameters are fixed at Optimizer: Adam, Loss: Cross-Entropy, Resize factor: 1/2, Transfer learning: Yes, Data augmentation: No. Overall the W48 achieved the best results and is picked as the backbone for the HRNet.



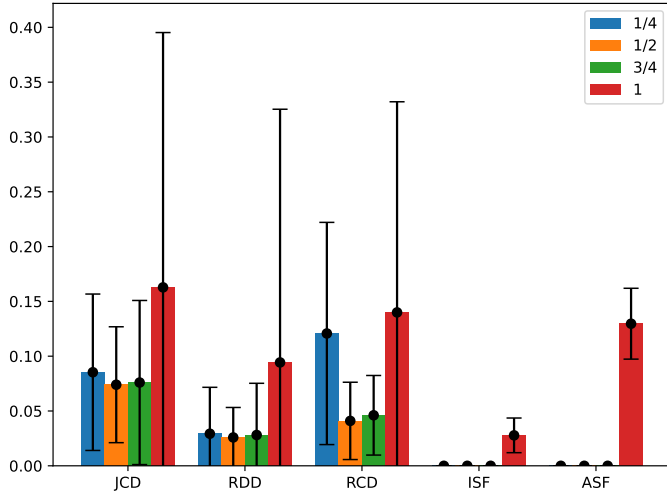
Extension	JCD	RDD	RCD	ISF	ASF
None	0.151	0.058	0.069	0.000	0.028
±	0.170	0.086	0.084	0.000	0.016
Transfer learning	0.078	0.028	0.043	0.000	0.000
±	0.058	0.034	0.037	0.000	0.000
Data augmentation	0.121	0.048	0.050	0.000	0.000
±	0.130	0.072	0.066	0.000	0.000
Transfer learning & Data augmentation	0.074	0.026	0.041	0.000	0.000
±	0.053	0.027	0.035	0.000	0.000

FIG. 6. Values of evaluation metrics for different extensions of the training data set, which is used by the U-Net. Bold values are the best values compared to the other results of one metric. The other hyperparameters are fixed at Backbone: ResNet 34, Optimizer: Adam, Loss: Cross-Entropy, Resize factor: 1/2. The accuracy of the U-Net is highest when transfer learning and data augmentation is used.



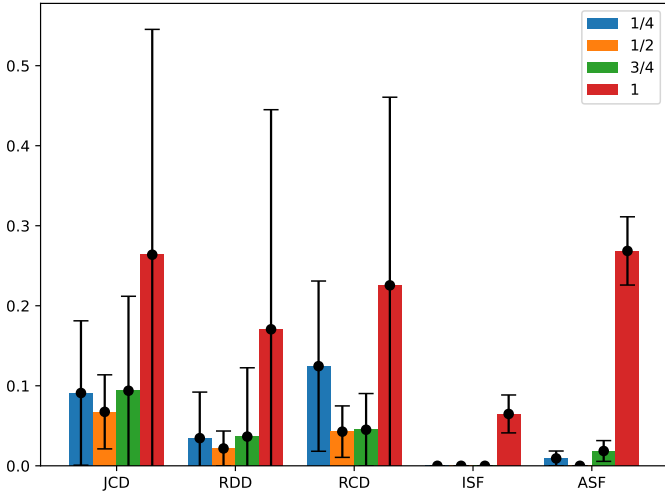
Extension	JCD	RDD	RCD	ISF	ASF
None	0.169	0.078	0.071	0.000	0.019
±	0.196	0.135	0.103	0.000	0.013
Transfer learning	0.109	0.041	0.062	0.000	0.009
±	0.123	0.069	0.082	0.000	0.009
Data augmentation	0.113	0.040	0.043	0.000	0.000
±	0.115	0.052	0.040	0.000	0.000
Transfer learning & Data augmentation	0.067	0.022	0.043	0.000	0.000
±	0.046	0.022	0.032	0.000	0.000

FIG. 7. Values of evaluation metrics for different extensions of the training data set, which is used by the HRNet. Bold values are the best values compared to the other results of one metric. The other hyperparameters are fixed at Backbone: W48, Optimizer: Adam, Loss: Cross-Entropy, Resize factor: 1/2. The accuracy of the HRNet is highest when transfer learning and data augmentation is used.



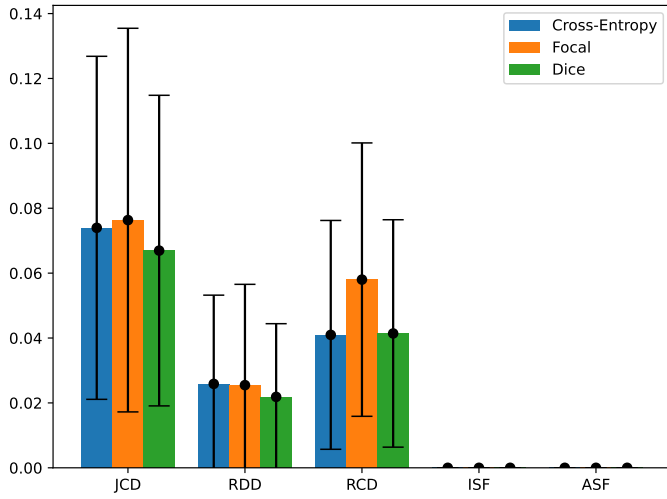
Resize factor	JCD	RDD	RCD	ISF	ASF
1/4	0.085	0.029	0.121	0.000	0.000
±	0.071	0.042	0.101	0.000	0.000
1/2	0.074	0.026	0.041	0.000	0.000
±	0.053	0.027	0.035	0.000	0.000
3/4	0.076	0.028	0.046	0.000	0.000
±	0.075	0.047	0.036	0.000	0.000
1	0.163	0.094	0.140	0.028	0.130
±	0.232	0.231	0.192	0.016	0.032

FIG. 8. Values of evaluation metrics for different image sizes. Bold values are the best values compared to the other results of one metric. The other hyperparameters are fixed at Backbone: ResNet 34, Optimizer: Adam, Loss: Cross-Entropy, Transfer learning: Yes, Data augmentation: Yes. The U-Net can achieve the highest accuracy when the original image size is reduced by half.



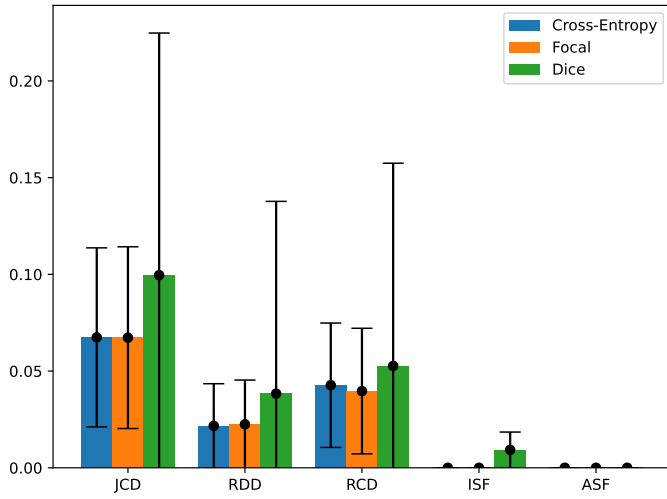
Resize factor	JCD	RDD	RCD	ISF	ASF
1/4	0.091	0.035	0.125	0.000	0.009
±	0.090	0.058	0.106	0.000	0.009
1/2	0.067	0.022	0.043	0.000	0.000
±	0.046	0.022	0.032	0.000	0.000
3/4	0.094	0.037	0.045	0.000	0.019
±	0.118	0.086	0.045	0.000	0.013
1	0.264	0.171	0.226	0.065	0.269
±	0.282	0.274	0.235	0.024	0.043

FIG. 9. Values of evaluation metrics for different image sizes. Bold values are the best values compared to the other results of one metric. The other hyperparameters are fixed at Backbone: W48, Optimizer: Adam, Loss: Cross-Entropy, Transfer learning: Yes, Data augmentation: Yes. The HRNet can achieve the highest accuracy when the original image size is reduced by half.



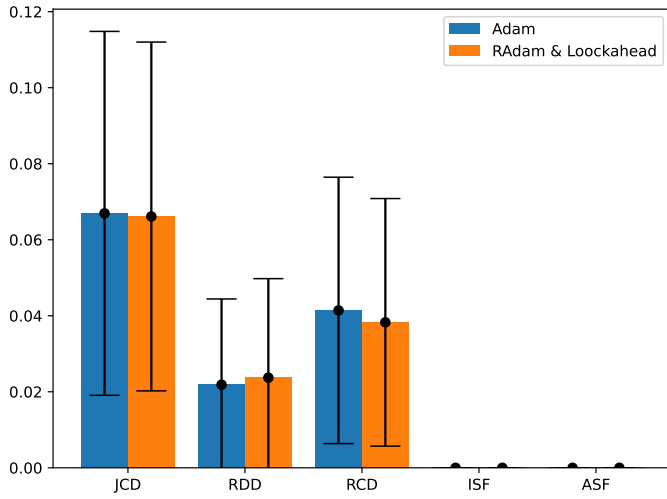
Loss function	JCD	RDD	RCD	ISF	ASF
Cross-Entropy	0.074	0.026	0.041	0.000	0.000
±	0.053	0.027	0.035	0.000	0.000
Focal	0.076	0.025	0.058	0.000	0.000
±	0.059	0.031	0.042	0.000	0.000
Dice	0.067	0.022	0.041	0.000	0.000
±	0.048	0.023	0.035	0.000	0.000

FIG. 10. Values of evaluation metrics for different loss functions, used by the U-Net. Bold values are the best values compared to the other results of one metric. The other hyperparameters are fixed at Backbone: ResNet 34, Optimizer: Adam, Resize factor: 1/2, Transfer learning: Yes, Data augmentation: Yes. The U-Net can achieve the highest accuracy when the Dice loss is used.



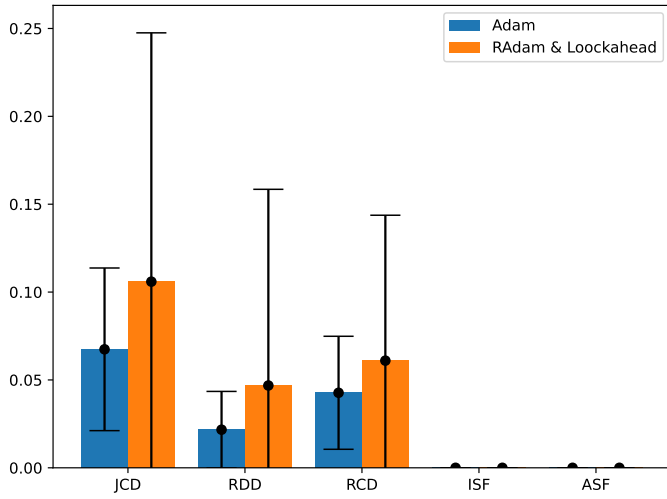
Loss function	JCD	RDD	RCD	ISF	ASF
Cross-Entropy	0.067	0.022	0.043	0.000	0.000
±	0.046	0.022	0.032	0.000	0.000
Focal	0.067	0.022	0.040	0.000	0.000
±	0.047	0.023	0.032	0.000	0.000
Dice	0.100	0.038	0.053	0.009	0.000
±	0.125	0.099	0.105	0.009	0.000

FIG. 11. Values of evaluation metrics for different loss functions, used by the HRNet. Bold values are the best values by compared to the other results of one metric. The other hyperparameters are fixed at Backbone: W48, Optimizer: Adam, Resize factor: 1/2, Transfer learning: Yes, Data augmentation: Yes. The HRNet can achieve the highest accuracy, if the Cross-Entropy or the Focal loss is used.



Optimizer function	JCD	RDD	RCD	ISF	ASF
Adam	0.067	0.022	0.041	0.000	0.000
±	0.048	0.023	0.035	0.000	0.000
RAdam & Loockahead	0.066	0.024	0.038	0.000	0.000
±	0.046	0.026	0.033	0.000	0.000

FIG. 12. Values of evaluation metrics for different optimizers, used by the U-Net. Bold values are the best values compared to the other results of one metric. The other hyperparameters are fixed at Backbone: ResNet 34, Loss: Dice, Resize factor: 1/2, Transfer learning: Yes, Data augmentation: Yes. The U-Net can achieve the highest accuracy when the optimization is done by RAdam combined with Loockahead.



Optimizer function	JCD	RDD	RCD	ISF	ASF
Adam	0.067	0.022	0.043	0.000	0.000
±	0.046	0.022	0.032	0.000	0.000
RAAdam & Lookahead	0.106	0.047	0.061	0.000	0.000
±	0.142	0.112	0.083	0.000	0.000

FIG. 13. Values of evaluation metrics for different optimizers, used by the HRNet. Bold values are the best values compared to the other results of one metric. The other hyperparameters are fixed at Backbone: W48, Loss: Cross-Entropy, Resize factor: 1/2, Transfer learning: Yes, Data augmentation: Yes. The HRNet can achieve the highest accuracy when the optimization is done by Adam.

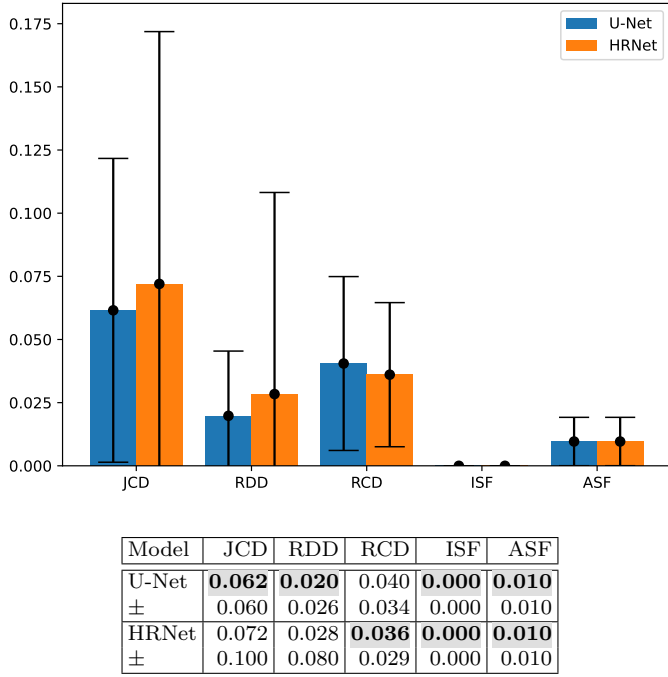


FIG. 14. Evaluation of the segmentation with the optimized U-Net and HRNet models on the test data set shows higher accuracy of the U-Net. The optimal hyperparameter configuration for the U-Net is Backbone: ResNet 34, Optimizer: RAdam & Lock-ahead, Loss: Dice, Resize factor: 1/2, Transfer learning: Yes, Data augmentation: Yes. The final hyperparameter configuration for the HRNet is Backbone: W48, Optimizer: Adam, Loss: Cross-Entropy, Resize factor: 1/2, Transfer learning: Yes, Data augmentation: Yes.

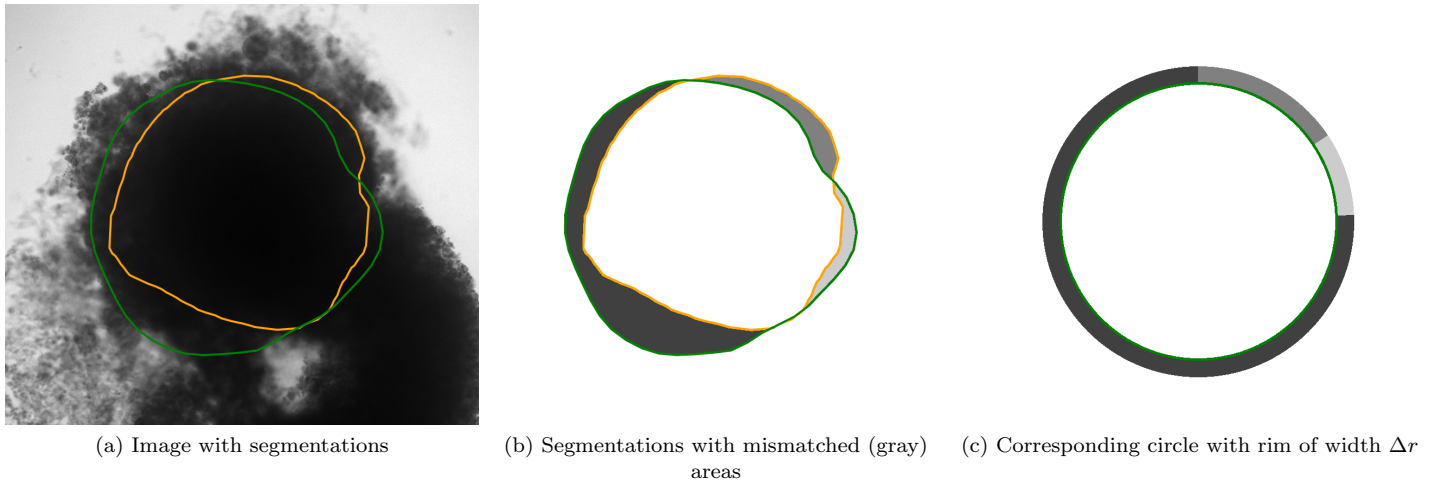
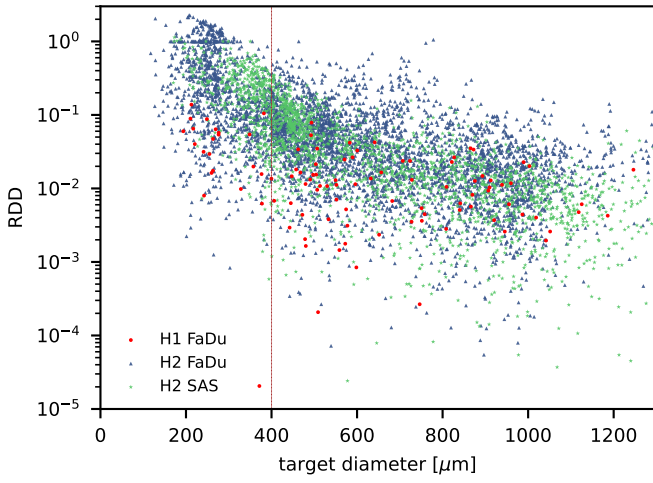
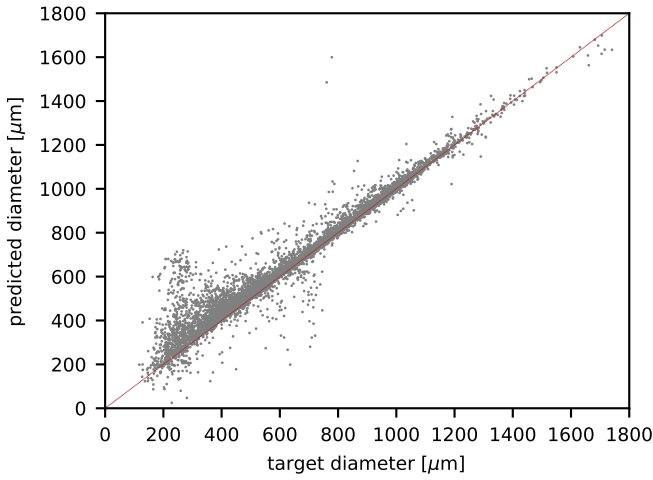


FIG. 15. Illustration of the average radial error Δr defined in Eq. (3) (example with large JCD > 0.2 for visibility). (a) Zoom of image from App. Fig. 3 with JCD = 0.24 with corresponding automatic (orange line containing predicted area P) and manual segmentation (green line containing target area T). (b) Segmentations from (a) with mismatched areas shown in gray (missing area $T \setminus P$ in bright and dark gray, additional area $P \setminus T$ in intermediate gray). (c) Circle (green line) and added rim (gray areas) with areas corresponding to (b): Area within green circle is equal to area within manual segmentation in (b) and gray areas within the adjacent rim are equal to corresponding mismatched areas in (b). Then the radial thickness of the rim is equal to the average radial error Δr defined in Eq. (3).



(a) RDD over spheroid diameter



(b) Comparison diameters from manual and automatic segmentation

FIG. 16. Validation based on diameter of automatic segmentation with the optimized U-Net on larger, independent data sets, analogous to Fig. 4. (a) RDD shows that majority of deviations are below 10% and higher deviations occur mostly below $d_T < 400 \mu\text{m}$. (b) Direct comparison of diameters (grey points) resulting from automatic segmentation (predicted diameter) and manual segmentation (target diameter) shows high accuracy (red line represents perfect match) with larger deviations mostly at $d_T < 400 \mu\text{m}$.